

1 **On the Nationwide Variability of Low-Level Jets Prior**
2 **to Warm-season Nocturnal Rainfall in China Revealed**
3 **by Radar Wind Profilers**

4 Ning Li^{a,b,c}, Jianping Guo^{a,d*}, Xiaoran Guo^{a,d}, Tianmeng Chen^{a,d}, Zhen Zhang^a, Na
5 Tang^a, Yifei Wang^a, Honglong Yang^d, Yongguang Zheng^c, Yongshui Zhou^e

6 ^a *State Key Laboratory of Severe Weather Meteorological Science and Technology &*
7 *Specialized Meteorological Support Technology Research Center, Chinese Academy*
8 *of Meteorological Sciences, Beijing 100081, China*

9 ^b *College of Earth and Planetary Sciences, University of Chinese Academy of*
10 *Sciences, Beijing 100049, China*

11 ^c *National Meteorological Centre, Beijing 100081, China*

12 ^d *CMA Field Scientific Experiment Base for Low-Altitude Economy Meteorological*
13 *Support of Unmanned Aviation in Guangdong-Hong Kong-Macao Greater Bay Area,*
14 *Shenzhen 518108, China*

15 ^e *Guizhou Meteorological Observatory, Guiyang 550001, China*

21 Correspondence to:

22 [Dr./Prof. Jianping Guo \(Email: jpguocams@gmail.com\)](mailto:jpguocams@gmail.com)

25

Abstract

26 Nocturnal rainfall initiation is closely linked to low-level jets (LLJs), but national-scale
 27 LLJ features over China—especially their evolution preceding warm-season nocturnal
 28 rainfall—remain unknown due to scarce high-resolution vertical observations. Here,
 29 we reveal the fine vertical structure of LLJs and their rapid evolution within 2 hours
 30 preceding the onset of nocturnal heavy rain (HR) and non-HR across four phases of
 31 rainy seasons in China during the warm season (April–October) of 2023–2024, utilizing
 32 data from a nationwide network of radar wind profilers (RWPs) in combination with
 33 surface observations and reanalysis data. Results show that nocturnal rainfall accounted
 34 for over 50% of warm-season rainfall, with 56% preceded by LLJs within 2 hours of
 35 its onset. In monsoon regions, ~45% of nocturnal HR were LLJ-associated (LLJ HR),
 36 producing heavier rainfall than non-LLJ HR events. Critically, LLJ HR events
 37 underwent a minute-scale ‘rapid reorganization’ of the LLJ structure, characterized by
 38 oscillatory evolution in jet height, frequency and strength. This creates a favorable
 39 environment for the ‘final-stage intensification’ of dynamic field during the last ~30
 40 min, where widespread intensification of jet—coupled with significant thermodynamic
 41 instability—act as a primary dynamical forcing mechanism, and a key precursor signal
 42 for HR initiation. In stark contrast, LLJ non-HR events exhibited quasi-steady or
 43 weakening dynamical trends, accompanied by an inadequate thermodynamic response
 44 that lacks such synergistic coupling. These findings demonstrate that minute-scale
 45 dynamic adjustments driven by swift evolution of the LLJ are essential for nocturnal
 46 HR, offering critical observational constraints for regional model parameterizations and
 47 nowcasting accuracy.

48

Deleted: al

Deleted: wind

Deleted: leading up to

Deleted: their

Deleted: approximately

Deleted: and

Deleted: ced

Deleted: s

Deleted: s

Formatted: Font color: Text 1

Deleted: the

Deleted: serves as a

Deleted: functions

Deleted: decisive triggering mechanism

Deleted: a

Formatted: Font color: Text 1, English (US)

Formatted: Font color: Text 1

Deleted: the initiation of

Deleted: is

Deleted:

Deleted: thereby providing

Formatted: English (US)

67

68

Short Summary

69 Nighttime rainfall often links to low-level jets (LLJs), but we lack clarity on nationwide
70 LLJ features. We here used a nationwide radar wind profiler network to study LLJ
71 changes 2 hours before rainfall, covering China's 2023–2024 rainy seasons. 56%
72 nighttime rainfall had LLJs. The LLJs-associated heavy rain needed a rapid adjustment
73 of LLJs' vertical structure, especially a significant intensification within 30 minutes
74 preceding rain. This shows the importance of LLJ in nowcasting rainfall.

75

76

77

78

79

80

81

82

83

Deleted: ¶

85 1. Introduction

86 Forecasting nocturnal heavy rainfall (HR) and associated severe convective
87 weather remains a major challenge in hazardous weather prediction (Davis et al., 2003;
88 Trier et al., 2006), owing to the complexity of triggering mechanisms, the scarcity of
89 continuous high-resolution observations, and inaccuracies in model parameterizations
90 (Carbone and Tuttle, 2008; Reif and Bluestein, 2017; Weckwerth et al., 2019; Zhao et
91 al., 2025). Crucially, the low-level jet (LLJ) that exhibit a diurnal cycle with a
92 maximum at night is widely recognized as a key contributor to nocturnal HR (Bonner
93 1968; Mitchell et al., 1995; Tuttle and Davis, 2006), as documented in regions or
94 countries such as the Great Plains of the United States (Maddox, 1983; Higgins et al.,
95 1997), Argentina (Marengo et al., 2004), India (Monaghan et al., 2010), North China
96 Plain (Li et al., 2024).

Formatted: Indent: First line: 2 ch, Space Before: 0 pt, After: 0 pt

97 The LLJs primarily originate from the inertial oscillations (IO) following the
98 sudden decay of turbulence after sunset (Blackadar, 1957) and thermal imbalances
99 induced baroclinicity over sloping terrain (Holton, 1967). Functioning as concentrated
100 corridors for heat, moisture, and momentum transport, LLJs can modulate the diurnal
101 oscillation in water vapor by IO (Rasmusson, 1967; Zhang et al., 2019) and enhance
102 convective instability, particularly when elevated high- θ_e air encounters frontal
103 boundaries (Trier et al., 2017). Also, strong low-level vertical wind shear (VWS)
104 associated with LLJs necessarily benefits deep lifting (Maddox et al., 1979; Stensrud,
105 1996; Rasmussen and Houze, 2016). These mechanisms collectively provide essential
106 thermodynamic and dynamic support for the initiation and organization of nocturnal
107 convection, especially where LLJs force low-level ascent at jet termini or via positive
108 vorticity advection left of the jet axis (Chen et al., 2017; Du and Chen, 2019; Xia and
109 Zhao, 2009).

Formatted: Space Before: 0 pt, After: 0 pt

110 Furthermore, LLJs interact synergistically with other key factors to trigger HR that
111 is associated with mesoscale convective systems (Chen et al. 2010; Chen et al., 2017;
112 Chen et al., 2024), including terrain effects (Anthes et al., 1982; Pan and Chen, 2019;
113 Huang et al., 2020), gravity waves (Weckwerth & Wakimoto, 1992), among others.

Formatted: Default Paragraph Font, Complex Script Font: Not Bold

Formatted: Space Before: 0 pt, After: 0 pt

114 These interactions are highly sensitive to the prevailing synoptic and subsynoptic-scale
115 environmental conditions (e.g., Hodges and Pu, 2019) and fine-scale structural of LLJs,
116 including LLJ frequency, spatial redistribution, and particularly localized wind profile
117 accelerations (Pitchford and London, 1962; Walters and Winkler, 2008; Du and Chen,
118 2019; Li et al., 2024). Understanding these intricate evolution features of LLJs is critical
119 for improving the forecasting of nocturnal HR.

120 Despite advances facilitated by regional reanalysis (e.g., Doubler et al., 2015; Li
121 et al., 2021), numerical modeling (e.g., Zhang and Meng, 2019), radiosonde
122 observations (e.g., Whiteman et al., 1997; Yan et al., 2020), and emerging artificial
123 intelligence techniques (e.g., Subrahmanyam et al., 2024) in understanding the
124 climatology and physical mechanisms of LLJs and their role in HR forecasting,
125 significant knowledge gaps remain. The insufficient spatiotemporal resolution of
126 conventional observing systems limits the ability to capture rapid pre-storm
127 environmental changes (Weisman et al., 2015; Cao et al., 2025; Roots et al., 2025),
128 thereby hindering systematic analysis of the fine-scale structure of LLJs and their
129 minute-scale evolution within the critical 2-hour window preceding rainfall.

130 Moreover, the mechanisms and impacts of LLJs exhibit considerable variation
131 across monsoon phases and geographic regions. As a classic monsoon climate region,
132 China exhibits particularly prominent nocturnal rainfall contributions across major
133 climate-sensitive areas (Yu et al., 2014), where LLJs play a crucial role in modulating
134 primary rainfall belts (Sun, 1986; Chen et al., 2010; Wang et al., 2013; Horinouchi et
135 al., 2019), such as those in Eastern China (Chen et al., 2017; Xue et al., 2018) and South
136 China (Du et al., 2020; Bai et al., 2021; Fu et al., 2021). However, nationwide
137 comparative studies examining LLJ precursor signals across different monsoon phases
138 in China are still lacking.

139 Radar wind profilers (RWPs) can offer transformative potential by capturing
140 minute-resolution wind profiles to reveal pre-rainfall dynamic precursors (Zamora et
141 al., 1987; Du et al., 2012; Molod et al., 2019; Guo et al., 2023). For example, Gebauer
142 et al. (2018) demonstrated the capability of RWPs to elucidate how heterogeneous
143 structures of LLJ trigger nocturnal convection in Great Plains; Based on a linear net of

Deleted: A critical shortcoming lies in the inability to capture minute-scale evolution of LLJs during the nocturnal pre-storm period. Conventional observing systems lack the spatiotemporal resolution required to resolve rapid changes in pre-storm environments

Deleted: t

Formatted: Space Before: 0 pt, After: 0 pt

150 RWPs deployed across the North China Plain, our previous study (Li et al., 2024)
151 observed rapid intensification of moisture flux convergence (MFC) driven by a surge
152 in LLJs profile within 30 min preceding nocturnal rainfall onset, highlighting the
153 sensitivity of RWP to minute-scale perturbations of LLJs profiles. However, it remains
154 an open question whether this minute-scale precursor is universally applicable across
155 diverse monsoon phases throughout mainland China. Furthermore, the systematic
156 differences in the fine-scale LLJ evolution that distinguish HR from non-HR have yet
157 to be fully elucidated.

158 Therefore, this study utilizes a nationwide network of RWPs to address the
159 following two questions: 1) How do the vertical structure of LLJs and their minute-
160 scale evolution within 0–2 hours preceding nocturnal rainfall vary across different rainy
161 season phases? and 2) What are the systematic differences in LLJ dynamic-
162 thermodynamic mechanisms between LLJ-influenced HR and non-HR events? The
163 remainder of this paper is structured as follows: Section 2 details data and methodology,
164 Section 3 presents comparative analyses of characteristics of rainfall and LLJs
165 evolution, and Section 4 synthesizes key conclusions.

166 **2. Data and Methodology**

167 *2.1 Radar wind profiler measurements*

168 The RWP observations collected from 31 stations across China (Fig.1) from April
169 to October in 2023–2024 were analyzed in this study, which can provide wind speed
170 and direction with a vertical resolution of 120 m and an interval of 6 minutes (Liu et al.,
171 2019). To reduce the potential influence of poor data quality, RWP data underwent
172 strict quality control following procedures proposed by Wei et al. (2014) and Miao et
173 al. (2018). Firstly, to minimize contamination from precipitation particles, which can
174 introduce significant errors in Doppler-based wind retrieval, all observations during
175 rainfall periods were removed. Secondly, within each profile below 3 km above ground
176 level (AGL), missing values and significant outliers that were defined as values
177 exceeding 2.5 standard deviations from the mean were removed. Next, for each profile,
178 if more than 40% of the data points below 3 km AGL were outliers or missing, that

Deleted: ↵

Formatted: Font: 12 pt, Complex Script Font: 12 pt, Pattern:
Clear

180 entire profile was discarded. Finally, discontinuous, or missing data points were
181 estimated using linear interpolation. Following this quality control process, 109,400
182 wind profiles were discarded and a total of 2,606,042 profiles across China were
183 available for analysis during the study period.

184 *2.2 Multi-source meteorological data*

185 In addition, 1-min rainfall measurements were directly acquired from the rain
186 gauge measurements at 2160 national weather stations across China to identify rainfall
187 events. Rainfall amounts were accumulated over 6-min intervals to ensure temporal
188 alignment with the RWP measurements. Ground-based meteorological variables are
189 measured at 1-min intervals from national weather stations, including 2-m air
190 temperature, relative humidity, and surface pressure. All ground-based data have
191 undergone rigorous quality control (China Meteorological Administration, 2020; Zhao
192 et al., 2024) and are publicly accessible at the National Meteorological Information
193 Center of China Meteorological Administration (CMA).

194 Furthermore, to diagnose large-scale circulation patterns and environmental
195 conditions preceding nocturnal rainfall influenced by LLJs, this study utilized
196 meteorological variables derived from the fifth generation of the European Centre for
197 Medium-Range Weather Forecasts atmospheric reanalysis (ERA5) of the global
198 climate (Hersbach et al., 2020). The ERA5 data features a horizontal resolution of
199 $0.25^\circ \times 0.25^\circ$ across 37 vertical pressure levels and hourly temporal resolution. Unless
200 otherwise specified, all datasets cover the study period of April to October in 2023–
201 2024.

202 *2.3 Identification of nocturnal rainfall events*

203 Firstly, days with typhoon activity were excluded. To minimize the impact of
204 rainfall on RWP measurements, a minimum dry interval of 2 hours was required
205 between consecutive rainfall events. Following the methodology of Li et al. (2024), a
206 rainfall occurrence was defined when the accumulated rainfall measured by all rain
207 gauges within a 25-km radius of each RWP station exceeded 0.1 mm. To account for

Deleted: total

Deleted: which was

Deleted: A

Deleted: ing

212 rainfall intermittency and filter out transient noise, a valid rainfall event required the
213 initial detection to be followed by at least two subsequent occurrences within 30 min.
214 Any isolated initial occurrence not meeting this criterion was discarded. Notably, this
215 25-km radius serves as a rigorous spatial constraint to not only mitigates the limitations
216 of single-gauge measurements but also ensures the onset of rainfall at this scale are
217 temporally coherent with that of the rain gauge co-located with RWP (as confirmed by
218 sensitivity tests in Fig. S1 and Table S1). This guarantees direct physical coupling
219 between local rainfall and the RWP-observed wind profiles.

220 Nocturnal rainfall events were defined as those occurring between 2000 and 0800
221 Local Standard Time (LST). Based on operational classifications from the National
222 Water Resources Bureau and CMA, the rainy season was categorized into four
223 consecutive phases: (1) the South China Pre-summer Rainy Season (April 1 to June 8,
224 2023 and April 1 to June 9, 2024), (2) the Meiyu Season (June 9 to July 14, 2023 and
225 June 10 to July 21, 2024), (3) the North China Rainy Season (July 15 to August 31,
226 2023 and July 22 to August 31, 2024), and (4) the West China Autumn Rainy Season
227 (September 1 to October 31 for both 2023 and 2024). These phases are subsequently
228 designated as Phase 1 to Phase 4 throughout this study. Four regions of interest (ROIs)
229 were subsequently selected for detailed analysis (see Table 1).

230 Further screening identified locally nocturnal HR events, where the mean 6-min
231 rainfall intensity exceeded the 75th percentile of all recorded rainfall events at each
232 station. This threshold can effectively distinguish significant HR from weak rainfall
233 while ensuring a sufficient sample size for robust statistical analysis of minute-scale
234 LLJ dynamics (Table S1). Furthermore, a sensitivity test by varying the thresholds to
235 85th and 95th percentile to ensure that the main conclusion regarding the precursory
236 signals of LLJs is robust within a reasonable threshold range (see Figs. S2–S5).

237 Statistical analysis revealed 3,155 nocturnal rainfall events during the 2023–2024
238 warm seasons (within the 31 red circles shown in Fig.1). Event counts per rainy season
239 phase were 1,109, 689, 652, and 705 respectively, with 841 events classified as
240 nocturnal HR events.

Formatted: Font: (Asian) SimSun, Complex Script Font: Bold, English (US)

Deleted: following initial detection

Deleted: ,

243 2.4 Identification of LLJs and associated rainfall event

244 To ensure identified LLJs exhibit significant vertical wind shear characteristic of
245 jet-like profiles, the following criteria are adopted: (1) a maximum horizontal wind
246 speed exceeding 10 m s^{-1} in the lowest 3 km AGL, and (2) a wind speed reduction of
247 at least 3 m s^{-1} from the maximum to minimum below 3 km AGL, or to 3 km AGL if
248 no minimum exists. These deliberately conservative wind speed thresholds maximize
249 LLJ sample size for enhanced statistical robustness. This definition standard has been
250 widely adopted in previous studies (Bonner, 1968; Whiteman et al., 1997; Du et al.,
251 2014; Yan et al., 2020). The strength of LLJ or jet nose is defined as the maximum wind
252 speed along the entire profile. The LLJ core height is defined as the altitude of the wind
253 speed maximum during LLJ occurrences. Correspondingly, the LLJ direction is
254 determined by the wind direction at the height of the LLJ.

255 We define rainfall events where LLJ occurs at least twice within 2 hours before rainfall
256 as an LLJ event (Li et al., 2024). The HR events influenced by LLJs (LLJ_HR events),
257 HR events without LLJ influence (non-LLJ_HR events), and non-HR events affected
258 by LLJ (LLJ_non-HR events) are further distinguished.

Formatted: Indent: First line: 0 cm

Deleted: ¶

259 3. Results and discussion

260 3.1 General characteristics of nocturnal rainfall and LLJs

261 Firstly, we characterized the spatiotemporal patterns of rainfall and LLJs observed
262 nationwide during the 2023-2024 warm season. Nationally, nocturnal rainfall
263 accounted for 50.9% of total warm-season rainfall, with pronounced concentrations
264 over North, Northeast and Southwest China (Figs. 2d and 2g). In contrast, the
265 pronounced daytime rainfall dominance in South China (Fig. 2a) may arise from the
266 interaction between enhanced onshore monsoonal flows and terrain (Bai et al., 2020),
267 sea breeze fronts and cold pool (Chen et al., 2016). In terms of frequency, nocturnal
268 rainfall occurred more frequently, constituting 52.5% of the total rainfall frequency
269 versus 47.5% for the daytime, with the highest nocturnal proportions found in
270 southwestern and eastern regions (Figs. 2e and 2h). Although the national mean rainfall

272 intensity was generally lower at night (1.2 mm/h) than during the day (1.8 mm/h; Figs.
273 2c and 2f), the probability of nocturnal HR occurrence was significant (51.3%),
274 particularly across western, North, and northeastern China (Fig. 2i).

275 Figure 3 displays the key attributes of LLJs detected at all 31 RWPs across China
276 using the criteria defined in Section 2. Nocturnal LLJ activity occurred more frequently,
277 with an overall occurrence frequency increase of nearly 18% relative to diurnal LLJs
278 (Figs. 3a and 3e). This pronounced nighttime enhancement is consistent with the
279 classical IO₄ mechanism, whereby reduced surface friction after sunset allows the
280 decoupled boundary layer to accelerate and form stronger LLJs. Spatially, both daytime
281 and nighttime LLJs were more prevalent in eastern and southeastern China, particularly
282 along the Yangtze River basin and coastal regions, where moisture-rich monsoonal
283 flows dominate. In contrast, lower frequencies were observed over northwestern China,
284 likely reflecting weaker large-scale moisture transport and reduced baroclinicity in arid
285 inland regions.

286 In terms of jet core height (Figs. 3b and 3f), nocturnal LLJs generally exhibited
287 slightly lower core altitudes compared to their daytime counterparts, with most cores
288 concentrated below ~1500 m. This lowering of the jet core at night is consistent with
289 boundary-layer stabilization and the formation of a shallow nocturnal inversion, which
290 confines the jet maximum to lower altitudes. Regarding jet intensity (Figs. 3c and 3g),
291 nighttime LLJs were typically stronger, with a higher proportion of stations reporting
292 wind speeds exceeding 16–18 m s⁻¹. The combination of enhanced wind speed and
293 reduced core height suggests a more concentrated and dynamically organized jet
294 structure during nighttime hours. The dominant wind directions (Figs. 3d and 3h)
295 further reflect regional circulation controls. Southeasterly and southwesterly LLJs
296 prevailed in eastern China, consistent with the transport of warm, moist air from the
297 South China Sea and western Pacific during the warm season. In northern and
298 northwestern regions, LLJs exhibited more variable directional characteristics, likely
299 influenced by synoptic-scale pressure gradients and topographic channeling effects.

Deleted: was

Deleted: China

Deleted: China

Deleted: s

Deleted: ies

Formatted: English (US)

Formatted: English (US)

Formatted: English (US)

Formatted: English (US)

305 Overall, Fig. 3 demonstrates that nocturnal LLJs are not only more frequent but
306 also stronger and lower in altitude than their daytime counterparts. These structural
307 differences imply enhanced moisture transport efficiency and greater potential for
308 nighttime convective organization, providing a dynamical foundation for the observed
309 diurnal asymmetry in heavy rainfall occurrence examined in subsequent sections.

310 Statistical analysis revealed a substantial linkage between LLJs and nocturnal
311 rainfall. Specifically, 56% of all nocturnal rainfall events across China were preceded
312 by the presence of LLJs within 2 hours, establishing nocturnal rainfall influenced by
313 LLJs as a major component of warm-season rainfall in China. This relationship was
314 strongly modulated by the seasonal migration of the western Pacific subtropical high
315 (WPSH), whose northward progression and subsequent retreat governed the latitudinal
316 displacement of HR belts and closely synchronized with the spatiotemporal evolution
317 of LLJ activity. The proportion of nocturnal rainfall events associated with LLJs during
318 the four rainy season phases reached 60.4%, 56.3%, 49.4%, and 54.9%, respectively
319 (solid-filled bars in Fig. 4a). Among 841 identified nocturnal HR events nationwide,
320 33.9%–47.2% were classified as LLJ_HR events across the four phases (diagonally
321 striped bars in Fig. 4a). This contrast between the high LLJ association for general
322 nocturnal rainfall and the more moderate fraction for HR indicates that, although LLJs
323 are a frequent precursor to rainfall, their presence alone does not guarantee the
324 occurrence of heavy rainfall.

325 A more detailed statistical analysis of ROIs revealed the key role of LLJ coupling
326 in primary rain belt regions of each phase. A total of 71, 49, 33, and 34 nocturnal HR
327 events were identified in these ROIs during the period from Phase 1 to Phase 4 (Fig.
328 4b). On average, nearly 45.0% of HR events in these regions were associated with LLJs
329 within 2 hours before onset. Spatial analysis further confirmed that these LLJ_HR
330 events consistently produced heavier rainfall intensities than non-LLJ_HR events (red
331 boxes in Fig. 5), particularly within the four ROIs (red boxes in Fig. 5). Nevertheless,
332 the non-LLJ_HR events exhibited spatially heterogeneous intensity distributions,
333 where localized maxima may occur in areas outside the primary rain belts. For instance,
334 during Phase 2 in ROI-3 (Fig. 5f), sporadic high-intensity events driven by deep cold

Deleted: Spatially, the regions exhibiting pronounced jet activity and high absolute wind speeds were collocated with those experiencing intense nocturnal rainfall, particularly over northern and eastern regions. Vertically, these jets manifest as intensified LLJ cores concentrated below 1 km AGL (Figs. 3f and 3g). This vertical restructuring likely responds to nocturnal surface cooling and IO. The dominant wind direction shifted to westerly, southerly or southwesterly flows at night across most regions, potentially driven by thermal contrasts within the monsoon circulation pattern and topographic forcing. ¶

Formatted: English (US)

Deleted: which drove corresponding shifts in HR belts that

Formatted: Font: (Asian) SimSun, Complex Script Font: Bold, English (US), Pattern: Clear (White)

Deleted: the percentages classified as LLJ_HR events ranged from 33.9% to 47.2%

Formatted: English (US)

Formatted: Font: (Asian) SimSun, Complex Script Font: Bold, English (US), Pattern: Clear (White)

Deleted: These results indicated that the mere presence of LLJs, while a frequent precursor to general nocturnal rainfall, is necessary but insufficient for HR.

Formatted: Font: (Asian) SimSun, Complex Script Font: Bold, English (US), Pattern: Clear (White)

Formatted: English (US)

Deleted: ¶

Deleted: However,

Formatted: Font: (Asian) SimSun, Complex Script Font: Bold, English (US), Pattern: Clear (White)

Deleted: spatial analysis of site-averaged rainfall intensity revealed that LLJ_HR events consistently produced heavier rainfall than non-LLJ_HR events

Deleted: identified in each phase

Deleted: T

359 trough system resulted in high site-averaged intensities even without LLJs, whereas in
360 ROI-2, the absence of LLJs typically corresponded to weaker frontal precipitation (Fig.
361 S6).

362 Furthermore, at the national scale, probability distributions of rainfall intensity
363 (Fig. 6) indicated that LLJ_HR events exhibited a **significantly higher** tail (≥ 2.0 mm/6
364 min) compared to non-LLJ_HR events during Phases 1 and 3. During Phases 2 and 4,
365 however, **the distributions of the two event types were comparable, with LLJ_HR**
366 **events showing slightly weaker intensities**. Regionally, rainfall intensities within the
367 key ROIs generally exceeded the national average, particularly for LLJ_HR events.
368 Specifically, ROI-1 and ROI-2 demonstrated significantly higher probabilities of
369 heavier rainfall (≥ 2.0 mm/6 min) **in LLJ_HR events**. **Notably, LLJ_HR events in**
370 **ROI-4 favored intensities near 0.5 and 2.8 mm/6 min, yet the overall probabilities of**
371 **heavier rainfall remained slightly lower than non-LLJ_HR events**. Despite the
372 relatively high frequency of LLJ_HR events in ROI-3 during Phase 3 (see the pie charts
373 in Fig. 6), **their probability of producing heavier rainfall was comparable to, rather**
374 **than substantially greater than** that of non-LLJ_HR events. **Moreover, this region**
375 **exhibited the sharpest decay in probability density for heavier rainfall among all regions**.
376 **This behavior suggests that, although LLJs occur frequently in this region and season,**
377 **their contribution to extreme rainfall intensity is not dominant. Instead, other non-LLJ**
378 **forcing mechanisms, such as topographic lifting and mesoscale convective systems,**
379 **may play an equally or more significant role in generating HR in ROI-3 during Phase**
380 **3**.

381 In summary, although LLJ_HR events **were generally associated with enhanced**
382 **rainfall intensities across most ROIs and most phases, only ~31.1% of all identified LLJ**
383 **events were ultimately classified as HR events (Fig. 4b)**. **This relatively low conversion**
384 **rate indicates that the mere presence of LLJs is not sufficient to produce HR. The**
385 **substantial number of LLJ_non-HR events implies that additional dynamic and**
386 **thermodynamic conditions must coexist with LLJs to trigger HR. In particular, factors**
387 **such as moisture transport efficiency, vertical wind shear configuration, atmospheric**
388 **stability, and mesoscale lifting mechanisms may modulate whether an LLJ evolves into**

Deleted: This reflected the dominant role of LLJ coupling in primary rain belts region.

Deleted: Furthermore, a total of 71, 49, 33, and 34 nocturnal HR events were identified in these ROIs during from Ph... [1]

Deleted: the distributions of the two event types were si... [2]

Deleted: LLJ_HR events in ...OI-1 and ROI-2 demonst... [3]

Deleted: Notably, d

Formatted ... [4]

Deleted: , ...ather than dominant over...substantially greater... [5]

Formatted: English (US)

Deleted: their probability of producing extreme rainfall... [6]

Deleted: ...hat of non-LLJ_HR events. Moreover, And... [7]

Deleted: T...is region also ...xhibited the sharpest decay... [8]

Deleted: These findings...his behavior suggests imply... [9]

Formatted: English (US)

Deleted: This suggests that

Deleted: (e.g.,...topographic lifting and/or...mesoscal... [10]

Deleted: LLJs may not represent the dominant mechani... [12]

Formatted ... [11]

Deleted: this particular region and season

Deleted: .

Deleted: favored

Deleted: exhibit

Deleted: higher...rainfall intensities across mostin... [13]

Deleted:

Deleted: the relatively high proportion of LLJ_non-HP... [15]

Formatted ... [14]

Formatted ... [16]

Deleted: percentage underscores

Deleted: in...ufficient to produce guarantee... [18]

Formatted ... [17]

Formatted ... [19]

Deleted: specific ...ynamic and thermodynamic... [20]

Deleted: associated with...LLJs are required... [22]

Formatted ... [21]

Formatted: English (US)

514 a heavy-rain-producing system. Therefore, a detailed further examination of the fine-
515 scale vertical structures of LLJs prior to rainfall onset is crucial to disentangle the
516 dynamical characteristics that distinguish HR-producing LLJs from non-HR cases, as
517 explored in the following sections.

518 3.2 Minute-scale evolution of LLJs preceding nocturnal heavy and non-heavy 519 rainfall

520 To elucidate the contrasting precursor characteristics of LLJs that lead to nocturnal
521 rainfall of differing intensities, this section examines fine-scale vertical structure and
522 continuous evolution of LLJs within 2 hours preceding both LLJ_HR and LLJ_non-HR
523 events during four phases in their respective ROIs. The results revealed the distinct
524 spatiotemporal variations in vertical structure and evolutionary patterns of LLJs
525 occurred across seasonal phases.

526 During Phase1 in ROI-1, LLJ_HR events exhibited a significant increase in
527 frequency starting 108 min before rainfall onset, reaching secondary peaks at -84 min
528 and -60 min, culminating in maximum frequency immediately preceding HR (Fig. 7a).
529 Meanwhile, the average wind profiles showed a rapid intensify trend from 48 min
530 before HR onset, with the jet core reaching its peak wind speed (about 12.2 m s^{-1}) and
531 its height distinctly decreased (Fig. 8a), although there is the transient weakening of jet
532 strength within 60-48 min preceding HR. These LLJs featured a bimodal vertical
533 distribution with frequent occurrence layers at 0.5-1 km and 1.5-2 km AGL. This
534 structure was characteristic of double low-level jets (DLLJs), where the coexistence of
535 the boundary layer jets (BLJs) and synoptic-system-related jets (SLLJs) generated a
536 deep layer of forced ascent via BLJ-exit convergence and SLLJ-entrance divergence.
537 This dynamical coupling significantly favors organized deep convection in ROI-1
538 (Uccellini and Johnson, 1979; Du and Chen, 2018; Du and Chen, 2019; Liu et al., 2020).
539 Note that the composite wind profile (Fig. 8a) does not show a distinct bimodal vertical
540 distribution due to smoothing from averaging. Detailed examination of wind profiles
541 revealed that approximately 40% of LLJ_HR events exhibited DLLJs, while only 20%
542 of LLJ_non-HR events showed such a structure. Therefore, LLJ_non-HR events lacked

Deleted: investigat

Deleted: ing

Deleted: ion into

Deleted: preceding

Deleted:

Deleted: identify the distinct dynamical characteristics that facilitate HR, as detailed in the following sections.

Deleted: distinguish the specific dynamical characteristics of LLJs that lead to HR.

Formatted: Font: (Asian) SimSun, Complex Script Font: Bold, English (US), Pattern: Clear (White)

Formatted: English (US)

Deleted: ¶

Formatted: Font: Cambria Math

Deleted: low-level jet

Deleted: s

555 this dynamic coupling, with jets predominantly confined to the single 0.5–1 km layer.
556 Although LLJ_non-HR events showed a gradual increase in frequency from –48 min,
557 along with strengthening winds prior to rainfall (Figs. 7e and 8e), these changes were
558 rather limited compared to the pronounced evolution seen in LLJ_HR events under a
559 background of overall lower frequency and weaker intensity. This steady and weak
560 dynamical structure failed to provide sufficient dynamic lifting to efficiently initiate
561 strong convection.

562 Both event types exhibited notably high frequencies and intensities of LLJs over
563 ROI-2 during Phase 2, yet their evolutionary dynamics diverged sharply. For LLJ_HR
564 events, a coherent oscillatory vertical reorganization of LLJs is evident (Figs. 7b and
565 8b). At the first stage, both LLJ frequency and wind speed maximum peaked (exceeding
566 12 m s^{-1}) at –120 min, with the core situated 1.5–2 km AGL. Subsequently, a rapid
567 descent of frequently occurring height of LLJs to below 1 km AGL occurred,
568 accompanied by a concurrent decline in frequency and profile intensity to a minimum
569 around 84–72 min preceding HR. Analysis of wind kinetic energy and its vertical
570 transport (see Eqs. 1 and 2 in supporting material) confirmed that the ‘sudden drop’
571 likely results from the downward momentum transfer (Fig. S7a and c), which can
572 efficiently enhance low-level disturbances and dynamic forcing and serve as an
573 effective indicator of HR 1–2 hours later (Liu et al. 2003; Fu et al., 2020). Following
574 this descent, a distinct recovery phase ensued from –60 min, where the frequency
575 increased reaching a secondary peak at –48 min and jet core re-ascended to 1–2 km
576 AGL. The LLJ profile strength re-intensified to about 11.4 m s^{-1} . This rise of the jet
577 core and secondary enhancement are likely tied to cold pool-LLJ interactions and
578 intensified upward motion or latent heat release in convective clouds (further discussed
579 in Section 3.3). In conclusion, this pattern suggests an intense internal dynamical
580 adjustment process. In comparison, LLJ_non-HR events lacked such low-level
581 momentum transfer signals (Fig. S7b and d) and maintained a quasi-steady state, with
582 consistent LLJs strength (near 11.8 m s^{-1}) and a preferred height range of 1–2 km AGL
583 (Fig. 8f). The LLJs frequency exhibited gradual changes, peaking weakly at 36 min
584 preceding rainfall before a subsequent rapid decrease (Fig. 7f). This pattern indicates

585 an absence of the rapid dynamical redistribution observed in LLJ_non-HR events.

586 During Phase 3 in ROI-3, LLJ_HR events exhibited a bimodal temporal
587 distribution in LLJ frequency, with prominent peaks at -96 min and -48 min (Fig. 7c).

588 The dominant LLJ height was centered between 1–1.5 km AGL. The wind profiles
589 showed a corresponding evolution where the maximum wind speed increased from
590 approximately 8.0 m s⁻¹ at -120 min to a first peak about 9.5 m s⁻¹ by -84 min.

591 ~~Following a transient weakening (-48 to -24 min), a secondary intensification occurred~~
592 ~~immediately preceding HR onset (Fig. 8c).~~ Conversely, LLJ non-HR events were

593 characterized by substantially lower LLJs frequency (around 20%) and a more diffuse
594 structure (Fig. 7g), with wind profiles exhibiting weaker intensification preceding

595 rainfall (Fig. 8g). ~~Consequently, the rapid reorganization and final intensification of~~
596 ~~LLJs appeared to be critical dynamical drivers for HR. However, despite the potential~~

597 ~~influences of regional thermodynamics and topography, the insufficient dynamical~~
598 ~~forcing from overall weaker wind profiles in ROI-3 remained the primary reason for its~~

599 ~~comparatively lower probability of heavier rainfall (≥ 2.0 mm/6 min).~~

600 During Phase 4 in ROI-4, LLJ_HR events exhibited a distinctive two-stage
601 intensification process. The wind profiles initially strengthened rapidly starting from -

602 120 min, reaching a primary peak of approximately 12.8 m s⁻¹ at -72 min (Fig. 8d),
603 coinciding with a secondary peak in LLJ frequency. Following a brief weakening (-60

604 to -48 min), a renewed and explosive intensification occurred from -48 min onwards,
605 continuing until rainfall onset. Throughout this period, the LLJ cores remained

606 concentrated between 0.5–1.5 km AGL (Fig. 7d). In sharp contrast, LLJ_non-HR
607 events displayed a pattern of premature peaking followed by decay. Both frequency and

608 intensity peaked earlier at -84 min, followed by general attenuation (Fig. 7h). By -48
609 min, weakened wind profiles stabilized into a double-core structure maintaining around

610 10 m s⁻¹, with distinct jet cores near 0.8 km and 1.7 km AGL (Fig. 8h). Crucially, in
611 the LLJ_non-HR event, this premature peak and the subsequent continuous attenuation

612 of the low-level wind field resulted in a lack of sustained dynamic forcing during the
613 critical pre-rainstorm stage, failing to trigger HR.

Deleted: It then reached a secondary peak near -48 min and displayed a characteristic transient weakening (-48 to -24 min), after which a rapid intensification resumed until HR occurred ...

Deleted: showing

Deleted: s

Deleted: Thus, the pronounced, rapid change and final intensification in LLJs likely reflect a key dynamical mechanism conducive to HR initiation. However, while other factors such as the regional thermodynamics and complex topography may contribute to rainfall intensity, the insufficient dynamic forcing stemming from the overall weaker wind profiles in ROI-3 served as the primary explanation for its lowest probability of heavier rainfall (≥ 2 mm/6 min) potentially explained the lower probability of heavier rainfall in LLJ_HR events over ROI-3 during Phase 3 relative to other regions and phases.

631 Synthesizing the evolution across all phases, although a distinct transient
632 weakening of ~~the~~ jet profile, was consistently observed, ~~LLJs exhibited a rapid re-~~
633 ~~intensification of wind speed accompanied by a lowering of the jet core height during~~
634 ~~approximately~~ the final 30 min ~~preceding~~ HR. ~~This recurring pre-rainfall adjustment~~
635 ~~suggests that LLJs underwent a short-term dynamical reorganization prior to HR onset.~~

636 We propose that this minute-scale oscillatory behavior—characterized by a
637 'weakening-then-strengthening' or 'descent-then-ascent' pattern—~~constitutes~~ a ~~robust~~
638 ~~dynamic precursor of~~HR. Physically, ~~the temporary weakening may reflect momentum~~
639 ~~redistribution or enhanced turbulent mixing, whereas the subsequent intensification and~~
640 ~~descent of the jet core likely enhance low-level moisture convergence and vertical wind~~
641 ~~shear, thereby strengthening upward motion and promoting convective development~~
642 ~~(Markowski & Richardson, 2010). Such rapid structural adjustment indicates that the~~
643 ~~timing and vertical evolution of LLJs, rather than their mere presence, play a critical~~
644 ~~role in modulating heavy rainfall production.~~

645 Furthermore, probability distributions of LLJ strength and height within 2 hours
646 preceding rainfall were compared across key regions (Fig. 9). During Phase 1 in ROI-
647 1, the strength of LLJs in LLJ_HR events was notably stronger by 2–3 m s⁻¹ than that
648 in LLJ_non-HR events (Fig. 9a). Height distributions showed distinct bimodal peaks
649 near 0.9 km and 1.75 km AGL (Fig. 9e). The average LLJs height was generally higher
650 in LLJ_HR events, which is usually affected by the coupling of the upper-level jet
651 stream or the ~~land-sea~~ breeze. During Phase 2 in ROI-2, LLJ_HR events showed higher
652 probabilities of strong LLJs (17–28 m s⁻¹) compared to the dominant 13 m s⁻¹ intensity
653 in LLJ_non-HR events (Fig. 9b). Influenced by large-scale circulation patterns, both
654 event types featured LLJs centered near 1.5 km AGL (Fig. 9f), though LLJ_HR events
655 developed a secondary maximum near 0.8 km AGL due to pre-rainfall descent of the
656 jet core (Fig. 7b). Contrastingly, Figure 9c shows that LLJ_HR events were associated
657 with weaker jet strengths (around 11 m s⁻¹) compared to LLJ_non-HR events (14–23
658 m s⁻¹) in ROI-3 during Phase 3, suggesting that strong LLJs don't necessarily induce
659 HR here. The height of LLJ in LLJ_HR events mainly concentrated near 1.2 km AGL,
660 whereas in LLJ_non-HR events, it was more uniformly distributed between 0–3 km

Deleted: s

Deleted: the

Deleted: consistently

Deleted: and

Formatted: Font: (Asian) SimSun, Complex Script Font: Bold, English (US), Pattern: Clear (White)

Deleted: the wind profiles of LLJs consistently showed a rapid increasing and height of core decreased in around

Deleted: before

Formatted: English (US)

Formatted: English (US)

Formatted: English (US)

Deleted: represent

Deleted: physically consistent

Deleted: signature of the dynamic environment adjustment essential for ...

Formatted: English (US)

Deleted: this phenomenon is likely attributable to the momentum consumption by developing convection or the flow blocking effect due to strong convergence

Deleted: Consequently, this rapid reorganization and final-stage intensification of the low-level dynamical field constitutes a decisive triggering mechanism for HR, standing in sharp contrast to the weaker, quasi-steady evolution observed in LLJ_non-HR events.

Formatted: English (US)

Deleted: sea-land

681 AGL with a higher probability nearly 1.5 km (Fig. 9g). For Phase 4 in ROI-4, LLJs
682 strength peaked near 15 m s^{-1} in both event types, but LLJ_HR events featured stronger
683 jets reaching $25\text{--}30 \text{ m s}^{-1}$ (Fig. 9d). The LLJs height in both events peaked
684 predominantly at 0.8 km AGL, with secondary peaks at 1.5 km for LLJ_HR and 2.0 km
685 AGL for LLJ_non-HR events (Fig. 9h).

686 In summary, although different internal dynamic adjustments, including frequency,
687 occurrence height, and wind profile intensity of LLJs, preceding LLJ_HR events were
688 observed due to the different dominant mechanisms influencing rainfall in each phase,
689 our findings highlight the role of fine-scale LLJ structures and their rapid vertical
690 reorganization in modulating nocturnal rainfall intensity, offering valuable insights for
691 improving regional nocturnal HR forecasting.

692 *3.3 Thermodynamic evolution associated with LLJs preceding nocturnal heavy* 693 *and non-heavy Rainfall*

694 The section 3.2 has clarified that the fine-scale dynamic characteristics of LLJs—
695 including their temporal evolution, vertical structure, and intensity variations—play a
696 pivotal role in modulating nocturnal rainfall intensity during rainy season phases.
697 However, the influence of LLJs on rainfall generation and intensification rarely
698 operates in isolation; instead, it depends strongly on the accompanying large-scale
699 thermodynamic environment, which provides the necessary moisture supply and
700 convective instability to sustain or amplify heavy rainfall. Thus, to fully unravel the
701 mechanisms underlying the distinction between LLJ_HR and LLJ_non-HR events, it is
702 essential to complement the dynamic analysis with an in-depth examination of the
703 thermodynamic conditions associated with LLJs within the immediate pre-convective
704 environment (within 1-hour preceding rainfall).

705 Further analysis of the large-scale thermodynamic conditions at 1 hour prior to
706 rainfall onset (Figs. 10 and 11) reveals consistently stronger thermal instability for
707 LLJ_HR versus LLJ_non-HR events, accompanied by stronger MFC within key
708 regions during each rainy season.

Deleted: ,

710 During Phase 1 in ROI-1, thermodynamic conditions were comparable between
711 event types. Southwesterly LLJs transported warm-moist air masses from the South
712 China Sea and Bay of Bengal, forming a pronounced warm-humid tongue (Fig. 10a and
713 10e). Coupled with MFC centers developing north of the jet axis (Fig. 11a and 11e),
714 this configuration facilitated nocturnal rainfall development. During Phase 2 in ROI-2,
715 LLJ_HR events exhibited a significantly stronger warm-moisture tongue with core θ_e
716 reaching 358 K—approximately 2 K higher than in non-HR events (Figs. 10b and 10f).
717 Dynamically, the stronger LLJ core (difference $>1.2 \text{ m s}^{-1}$) drove a sharper, continuous
718 band of MFC along the left flank of the jet axis (Fig. 11b), creating a robust triggering
719 mechanism for HR (Fig. 11b). During Phase 3 in ROI-3, intensified southwesterly LLJs
720 in HR events drove substantial northward transport of abundant moisture and higher θ_e
721 air (difference $>2 \text{ K}$) northward into a low θ_e environment (Fig. 10c), enhancing
722 convective instability. The synergistic interaction of this moist, high-energy advection
723 with orographic forcing from the Taihang Mountains generated intense MFC, with peak
724 values south of Beijing approximately $30 \times 10^5 \text{ km m}^{-2} \text{ s}^{-1}$ (Fig. 11c) larger than those
725 in LLJ_non-HR events, thereby driving nocturnal HR. Thermodynamic contrasts were
726 most pronounced during Phase 4 in ROI-4. Thermodynamic contrasts were most
727 pronounced during Phase 4 in ROI-4. LLJ_HR events featured a deep high- θ_e region
728 ($>356 \text{ K}$) over the southeastern Tibetan Plateau (Fig. 10d), contrasting with the cold
729 highs located to the northeast of ROI-4 and lower θ_e prevalent in LLJ_non-HR events
730 (Fig. 10h). Concurrently, accelerated easterly-southeasterly LLJs drove warm, moist air
731 towards the steep eastern Plateau margin. The impingement of this flow against the
732 sharp topographic gradient generated intense dynamic lifting and low-level
733 convergence. This mechanically forced ascent, synergizing with the abundant moisture
734 transport and strong MFC (Fig. 11h), played an essential role in triggering the observed
735 nocturnal HR in this region.

736 To elucidate the rapid processes leading to occurrence of rainfall, the minute-scale
737 evolution of key thermodynamic and dynamic parameters was further analyzed (Fig.
738 12), including surface θ_e , LLJ index and VWS. Specifically, LLJ index is defined as the
739 ratio of maximum wind speed below 3 km to the height where wind first exceeds 10 m

Deleted: difference

Deleted: -

Deleted: -

Deleted: -

744 s⁻¹. A rapid rise in LLJ index will reflect the extension and pulsing intensity of the LLJ,
745 and its magnitude has been shown to be positively correlated with subsequent rainfall
746 intensity 1–2 hour later (Liu et al., 2003). VWS is calculated as the wind speed
747 difference between the surface and jet height divided by the jet height and is used to
748 characterize the bulk shear from the surface to the jet layer associated with the
749 dynamical forcing and organization of convection (Wei et al., 2014).

Deleted: .

750 Figure 12a illustrates that during Phase 1 in ROI-1, despite the similarity in large-
751 scale environments between LLJ_HR and LLJ_non-HR events, they exhibited distinct
752 differences in the continuous evolution of LLJ-associated thermodynamic conditions
753 preceding rainfall onset. LLJ_HR events exhibited abrupt thermodynamic enhancement
754 from 90 min preceding the onset of rainfall driven by rapid intensification of LLJs, with
755 surface θ_e and VWS surging approximately 1.5 K and 0.005 s⁻¹ respectively.
756 Concurrently, the LLJ index surged from approximately 0.05 to 0.08 and VWS peaked
757 sharply at -60 min, signaling LLJs intensification and core descent (Figs. 7a, 8a). This
758 rapid, minute-scale co-intensification of thermodynamic and dynamic processes serves
759 as a critical precursor triggering HR. In contrast, LLJ_non-HR events showed weaker
760 increases of θ_e and VWS and a declining LLJ index (by about 0.02) alongside rising jet
761 cores, reducing low-level shear and convergence efficiency, thereby diminishing
762 overall rainfall intensity.

Deleted: s

Deleted: -

763 During Phase 2 in ROI-2, the thermodynamic environment displayed a distinct
764 ‘weakening-reintensification’ pattern (Fig. 12b), which aligns precisely with the
765 intrinsic dynamical adjustments of the wind field presented in Fig. 8b. Initially, at -120
766 min, concurrent peaks in the LLJ index and VWS were observed, coupled with a high
767 surface θ_e of 348.3 K. During the subsequent transition period, a drastic elevation in the
768 jet core height starting from -84 min caused a precipitous drop in the LLJ index. The
769 timing of this rapid evolution suggests a transient optimal window for nocturnal rainfall
770 triggering that is characteristic of LLJ_HR events in ROI-2. Following this, rapid
771 surface cooling began 60 min prior to HR. This cooling was likely induced by the cold
772 pool outflows associated with alternation or propagation of convective systems
773 embedded within the Mei-Yu front cloud system (Zhang et al., 2023). The resulting

Deleted: outflow of

778 dense cold air wedging beneath the strong southwesterly LLJs can lift the jet axis above
779 the cold-pool interface, further enhancing uplift and promoting rainfall (Luo et al.,
780 2014). This in turn facilitated the final re-intensification of the jet structure (Fig. 7b and
781 8b). ~~Crucially, this reorganized configuration~~ sharply enhances low-level vertical wind
782 shear and horizontal convergence (Fig. 12b), further promoting HR development. ~~In~~
783 ~~contrast,~~ LLJ non-HR events ~~exhibited~~ weaker thermodynamic support and diminished
784 dynamic forcing with consistently lower LLJ indices within 60 min preceding rainfall,
785 resulting in insufficient lift to sustain HR. Compared with the disordered fluctuations
786 of the LLJ non-HR events, ~~LLJ HR events highlight~~ the importance of thermal-
787 dynamic synergy influenced by LLJs evolution. ~~Even though the LLJ evolution may be~~
788 ~~modulated by convective feedback, the resulting reorganized jet profile still can serve~~
789 ~~as a robust dynamical precursor essential for triggering local HR.~~

790 During Phase 3 in ROI-3, LLJ_HR events featured prominent thermal
791 compensation (surface $\Delta\theta_e > 1\text{K}$, 850hPa $\Delta\theta_e > 2\text{K}$ versus non-HR events)—despite
792 possessing generally weaker dynamical forcing compared to other phases (Fig. 12c).
793 Temporally, the evolution was marked by distinct pulsations: The LLJ index exhibited
794 a rapid rise (from ~ 0.03 to ~ 0.06) starting 84 min prior to HR onset (Fig. 12c) driven
795 by a surge of LLJs profiles, while VWS peaked synchronously with the maximum LLJ
796 frequency. Subsequently, a secondary peak in both the LLJ index and VWS was
797 observed between -60 and -48 min. Although the subsequent declines in wind speed
798 and frequency led to notable fluctuations in these parameters, the VWS and LLJ index
799 underwent substantial intensification (with VWS increasing by $\sim 1.5\text{ s}^{-1}$) in the final 24
800 min, driven by the rapid acceleration of the LLJ wind field. This co-evolution with rapid
801 surface warming (increase of 0.25 K) released convective instability and enhanced
802 convergence (Fig. 10). Nevertheless, the overall weaker dynamical conditions likely
803 limited the depth and organization of convection, ~~potentially accounting for~~ the reduced
804 probability of heavier rainfall compared to other phases. In contrast, during LLJ non-
805 HR events, the LLJ index (~ 0.03) and θ_e vary rather gradually.

806 During Phase 4 in ROI-4, under the favorably thermal environments ($\theta_e > 346\text{ K}$),
807 LLJ_HR events showed a two-stage dynamic intensification. Initially, the LLJ index

Deleted: ed

Deleted: Importantly, this configuration

Formatted: Font: (Asian) SimSun, Complex Script Font: Bold, English (US)

Deleted: For

Deleted: ,

Deleted: ed

Deleted: these results

Deleted: emphasiz

Deleted: ed

Deleted: in triggering HR

Formatted: Font: (Asian) SimSun, Complex Script Font: Bold, English (US)

Formatted: Font: (Asian) SimSun, Complex Script Font: Bold, English (US)

Deleted: feedbacks

Deleted: ,

Formatted: Font: (Asian) SimSun, Complex Script Font: Bold, English (US)

Deleted: (

Deleted: explaining

821 surged, while the VWS and jet intensity reached synchronous secondary peaks at -72
822 min. In the second stage, VWS increased rapidly by ~0.9 (Fig. 12d), and the LLJ index
823 maintained an overall upward trend, peaking immediately prior to onset due to the
824 surging jet. But LLJ_non-HR events showed weakening trends in both dynamic and
825 thermodynamic conditions during the final 30 min and exhibited weaker changes
826 ($\Delta VWS < 0.45 \text{ s}^{-1}$, $\Delta LLJ \text{ index} < 0.02$), reflecting an absence of the coordinated
827 intensification necessary to initiate and sustain HR.

828 Although the evolution paths of the thermodynamic environment vary across
829 different phases, a universal cross-region precursor emerges: the LLJ index and VWS
830 consistently exhibits a strengthening or stabilizing trend in the final approximately 30
831 min preceding HR onset, operating in concert with significant low-level warming
832 (rising θ_e). In contrast, non-HR events generally lack this culminating dynamical
833 intensification. Overall, these results adequately showcase the sensitivity of regional
834 HR to the fine-scale structural evolution of LLJs and their coupling with
835 thermodynamic environments.

836 4. Summary and concluding remarks

837 Using wind profile measurements from a nationwide network of 31 RWP during
838 the warm seasons (April–October) of 2023–2024, this study characterized the minute-
839 scale evolution of LLJs as dynamic precursors to nocturnal rainfall across China. By
840 systematically comparing the vertically resolved structure and temporal evolution of
841 LLJs within the 2-hour window preceding nocturnal HR and non-HR events across four
842 distinct rainy-season phases, we identified the key dynamic-thermodynamic
843 distinctions governing rainfall intensity.

844 At the national scale, nocturnal rainfall accounted for nearly half of the total warm-
845 season precipitation, and 56% of nocturnal rainfall events were preceded by LLJs
846 within 2 hours. In the key regions of interest (ROIs), approximately 45.0% of identified
847 HR events were associated with LLJs. Overall, LLJ-related events were significantly
848 more prone to producing heavier rainfall than non-LLJ events across most regions,
849 underscoring the strong coupling between LLJs and nocturnal HR.

Formatted: Indent: First line: 2 ch

Deleted: ¶

Deleted: W

Deleted: were utilized to

Deleted: behaviors

Deleted:

Deleted: this study

Deleted: elucidates

Deleted: elucidated

Deleted: critical

Deleted: related to LLJs distinctions

Deleted: Statistical analysis revealed that

Deleted: a

Deleted: with

Deleted: these

Deleted: exhibiting

Deleted: influence

Deleted: the preceding

Deleted: Generally

Deleted: these

Deleted: key

Deleted: exhibited a significantly higher probability of
exhibited a distinct probability advantage in producing
heavier rainfall intensities compared to non-LLJ events,

Deleted: linkage

874 ~~Despite regional differences in synoptic forcing, consistent contrast in LLJ~~
875 ~~evolution were observed between HR and non-HR events across all phases. During~~
876 ~~Phase 1 in ROI-1, a bimodal vertical distribution of LLJs and their rapid~~
877 ~~thermodynamic-dynamic co-intensification starting 84 min prior to rainfall were~~
878 ~~identified as key precursors of LLJ_HR events, in sharp contrast to the decoupled~~
879 ~~dynamics of LLJ_non-HR events. Phase 2 (ROI-2) was characterized by a distinct~~
880 ~~oscillatory process, where HR events featured a rapid descent of the LLJ core below 1~~
881 ~~km followed by a robust rebound, distinguishing them from the quasi-steady state of~~
882 ~~LLJ_non-HR cases. In Phase 3 (ROI-3), LLJ_HR events exhibited significant thermal~~
883 ~~compensation and bimodal pulsations (peaks at -96 and -48 min), with a critical final-~~
884 ~~stage intensification serving as the decisive trigger. Similarly, Phase 4 (ROI-4) featured~~
885 ~~a distinctive two-stage intensification, where a rapid LLJ surge within 48 min of onset~~
886 ~~distinguished LLJ_HR events from the significantly attenuated dynamical structures of~~
887 ~~LLJ_non-HR events.~~

888 Although the ~~detailed~~ dynamical pathways vary ~~among~~ phases, ~~a unifying feature~~
889 ~~emerges~~: all LLJ_HR events exhibit a ~~'final-stage intensification'~~ of ~~low-level~~
890 ~~dynamics—manifested as enhanced LLJ strength, vertical wind shear, and LLJ index—~~
891 ~~within approximately 30 min preceding rainfall, occurring in synergy with increasing~~
892 ~~thermodynamic instability (e.g., rising equivalent potential temperature, θ_e). This result~~
893 ~~confirms~~ the universality of the final-stage low-level dynamic ~~amplification identified~~
894 ~~in our previous study (Li et al., 2024) and demonstrates its national-scale applicability~~
895 ~~across diverse monsoon regimes.~~

896 Crucially, ~~this study further~~ identifies a ~~previously under-resolved~~ ~~'preparatory~~
897 ~~adjustment'~~ phase ~~occurring 30–120 minutes prior to rainfall onset, during which LLJ~~
898 ~~frequency, strength and core height undergo systematic minute-scale reorganization.~~
899 This national-scale ~~evidence indicates~~ that the final dynamic trigger is contingent upon
900 this earlier synergistic coupling of minute-scale jet ~~structural~~ evolution and
901 thermodynamic destabilization. ~~This rapid, synergistic reorganization represents a~~
902 ~~necessary precondition for HR generation and contrasts sharply with the comparatively~~
903 ~~steady evolution observed in LLJ_non-HR events. These results highlight that the~~

Deleted: Pronounced

Deleted: LLJ evolution were

Deleted: ly

Deleted:

Deleted: , despite regional variations in synoptic forcing

Deleted: specific

Deleted: across different

Deleted: “

Deleted: ”

Formatted: English (US)

Deleted: the LLJs (LLJs strength, VWS and LLJ index) specifically within the 30 min preceding rainfall in syn... [23]

Formatted: English (US)

Deleted: can

Deleted: intensification

Deleted: observed

Deleted: analysi

Deleted: s

Formatted: English (US)

Deleted: as a robust trigger for nocturnal HR across di... [24]

Deleted: however,

Deleted: e current work

Deleted: novel

Deleted: “

Deleted: ‘

Deleted: ”

Deleted: ’

Deleted: (

Deleted:)

Deleted: for LLJs structure (

Deleted: s

Deleted:) that was not fully resolved in the regional study

Formatted: English (US)

Deleted: analysis reveals

Formatted: English (US)

939 occurrence and intensity of nocturnal rainfall are governed not simply by LLJ presence,
940 but by the fine-scale vertical evolution of LLJs and their interaction with regional
941 thermodynamic conditions.

942 Overall, this study establishes robust dynamic-rainfall linkages associated with
943 LLJs across different warm-season rainy periods in China. Future research should: (1)
944 expand multi-source observations to establish dynamic thresholds for early forecasting
945 systems of nocturnal rainfall, and (2) develop quantitative frameworks relating LLJ
946 structural evolution to rainfall intensity, offering theoretical support for optimizing
947 physical processes in LLJ parameterization schemes within high-resolution numerical
948 models. Further investigation is also needed to clarify the physical mechanisms
949 controlling rapid adjustments in LLJ core height and strength immediately prior to
950 rainfall onset.

951 Data Availability

952 The LLJs retrieved from the RWP network can be acquired from
953 <https://doi.org/10.5281/zenodo.17176759> (Li and Guo, 2025). The data from the
954 weather station are obtained from the China Meteorological Data Service Centre at
955 <https://data.cma.cn/en>, and the original ERA5 reanalysis data used here are available
956 from the ECMWF in Hersbach et al. (2020).

957 Acknowledgments

958 This work was supported by the National Natural Science Foundation of China
959 under grant 42325501, the Science and Technology Supporting Project of Guizhou
960 Province ([2023]236) and the National Key Research and Development Program of
961 China under grant 2024YFC3013001. Last but not least, we appreciated tremendously
962 the constructive comments and suggestions made by the anonymous reviewers that
963 significantly improved the quality of our manuscript.

964 Author Contributions

965 The study was completed with close cooperation between all authors. JG designed
966 the research framework; NL performed the analysis and drafted the original manuscript

Deleted: This coupled “rapid reorganization” process constitutes the essential, nationally valid precondition for HR generation, contrasting with the quasi-steady evolution observed in LLJ_non-HR events. This underscores that the occurrence and intensity of nocturnal rainfall are ultimately regulated by regionally specific thermo-dynamic interactions modulated by the evolution of fine vertical structure of the LLJ. ¶

Deleted: T

Deleted: distinct

Deleted: Additionally, the physical mechanisms governing evolution of LLJs height or strength immediately preceding rainfall onset require further investigation.

Formatted: English (US)

Field Code Changed

Field Code Changed

Field Code Changed

Deleted: G

Deleted: s

Deleted: of

Deleted: by

984 with contribution from JG; JG, XG, ZZ, YZ. JG, NT, YW, and YZ helped revise the
985 manuscript.

986 **Completing interests**

987 The authors declare that they have no conflict of interest.

988

989 **References**

- 990 Anthes, R. A., Kuo, Y. H., Benjamin, S. G., and Li, Y. F.: The evolution of the mesoscale
991 environment of severe local storms: Preliminary modeling results, *Mon. Weather*
992 *Rev.*, 110(9), 1187-1213, doi:10.1175/1520-0493(1982)110,1187:
993 TEOTME.2.0.CO;2, 1982.
- 994 Bai, L., Chen, G., Huang, Y., and Meng, Z.: Convection initiation at a coastal rainfall
995 hotspot in South China: Synoptic patterns and orographic effects, *J. Geophys. Res.*
996 *Atmos.*, 126(24), e2021JD034642, doi: 10.1029/2021JD034642, 2021.
- 997 Blackadar, A. K.: Boundary layer wind maxima and their significance for the growth
998 of nocturnal inversions, *Bull. Am. Meteorol. Soc.*, 38(5), 283-290,
999 doi:10.1175/1520-0477-38.5.283, 1957.
- 1000 Bonner, W. D.: Climatology of the low-level jet, *Mon. Weather Rev.*, 96(12), 833-850.
1001 doi:10.1175/1520-0493(1968)096<0833:COTLLJ>2.0.CO;2, 1968.
- 1002 Cao, Q., J. Guo, C. Xue, Z. Li, H. Xu, N. Li, Y. Sun, Z. Zhang, Y. Wang, J. Chen, Y.
1003 Zhou, and T. Chen: Divergent Sounding-derived Precursor Pathways Enable
1004 Discrimination of Dry versus Wet Severe Convective Winds. *Geophysical*
1005 *Research Letters*, 52, e2025GL117491. <https://doi.org/10.1029/2025GL117491>,
1006 2025.
- 1007 Carbone, R. E., and Tuttle, J. D.: Rainfall occurrence in the US warm season: The
1008 diurnal cycle, *J. Clim.*, 21(16), 4132-4146, doi:10.1175/2008JCLI2275.1, 2008.
- 1009 Chen, G., Sha, W., Iwasaki, T., and Wen, Z.: Diurnal Cycle of a Heavy Rainfall
1010 Corridor over East Asia, *Mon. Weather Rev.*, 145(8), 3365-3389,
1011 doi:10.1175/mwr-d-16-0423.1, 2017.
- 1012 Chen, H., Zhou, T., Neale, R. B., Wu, X., and Zhang, G. J.: Performance of the new
1013 NCAR CAM3. 5 in East Asian summer monsoon simulations: Sensitivity to
1014 modifications of the convection scheme, *J. Clim.*, 23(13), 3657-3675,
1015 doi:10.1175/2010JCLI3022.1, 2010.
- 1016 Chen, T., Guo, J., Guo, X., Zhang, Y., Xu, H., and Zhang, D.-L.: On the multiscale
1017 processes leading to an extreme gust wind event in East China: Insights from radar

1018 wind profiler mesonet observations. *Journal of Geophysical Research:*
1019 *Atmosphere*, 129, e2024JD041484, doi: 10.1029/2024JD041484, 2024.

1020 Chen, X., F. Zhang, and K. Zhao: Diurnal Variations of the Land-Sea Breeze and Its
1021 Related Precipitation over South China. *J. Atmos. Sci.*, 73, 4793 - 4815,
1022 doi:10.1175/JAS-D-16-0106.1, 2016.

1023 Chen, Y. L., and Li, J.: Large-scale conditions favorable for the development of heavy
1024 rainfall during TAMEX IOP 3, *Mon. Weather Rev.*, 123(10), 2978-3002, 1995.

1025 China Meteorological Administration: Specification for Automatic Observation of
1026 Ground Meteorology. China Meteorological Press, 2020.

1027 Davis, C. A., Maning, W. K., Carbone, R., Trier, S., and Tuttle, J.: Coherence of warm-
1028 season continental rainfall in numerical weather prediction models, *Mon. Weather*
1029 *Rev.*, 131, 2667-2679, doi:10.1175/1520-
1030 0493(2003)131<2667:COWCRI>2.0.CO;2, 2003.

1031 Dong, F., Zhi, X., Zhang, L., and Ye, C.: Diurnal variations of coastal boundary layer
1032 jets over the northern South China Sea and their impacts on diurnal cycle of
1033 rainfall over southern China during the early-summer rainy season, *Mon. Weather*
1034 *Rev.*, 149(10), 3341-3363, doi:10.1175/MWR-D-20-0292.1, 2021.

1035 Doubler, D. L., Winkler, J. A., Bian, X., Walters, C. K., and Zhong, S.: An NARR-
1036 derived climatology of southerly and northerly low-level jets over North America
1037 and coastal environs, *J. Appl. Meteorol. Climatol.*, 54(7), 1596-1619,
1038 doi:10.1175/JAMC-D-14-0311.1, 2015.

1039 Du, Y., and Chen, G.: Heavy Rainfall Associated with Double Low-Level Jets over
1040 Southern China. Part II: Convection Initiation, *Mon. Weather Rev.*, 147(2), 543-
1041 565, doi:10.1175/mwr-d-18-0102.1, 2019.

1042 Du, Y., and G. Chen: Heavy Rainfall Associated with Double Low-Level Jets over
1043 Southern China. Part I: Ensemble-Based Analysis, *Monthly Weather Review*, 146,
1044 3827 - 3844, doi: 10.1175/MWR-D-18-0101.1, 2018.

1045 Du, Y., Chen, G., Han, B., Bai, L., and Li, M.: Convection initiation and growth at the
1046 coast of South China. Part II: Effects of the terrain, coastline, and cold pools, *Mon.*
1047 *Weather Rev.*, 148(9), 3871-3892, doi:10.1175/MWR-D-20-0090.1, 2020.

Field Code Changed

1048 Du, Y., Zhang, Q., Ying, Y., and Yang, Y.: (2012). Characteristics of low-level jets in
1049 Shanghai during the 2008-2009 warm seasons as inferred from wind profiler radar
1050 data, *J. Meteorol. Soc. Jpn. Ser. II*, 90(6), 891-903, doi:10.2151/jmsj.2012-603,
1051 2012.

1052 Fu, S. M., Jin, S. L., Shen, W., Li, D. Y., Liu, B., & Sun, J. H.: A kinetic energy budget
1053 on the severe wind production that causes a serious state grid failure in Southern
1054 Xinjiang China, *Atmospheric Science Letters*, 21(7), e977, 2020.

1055 Gebauer, J. G., Shapiro, A., Fedorovich, E., and Klein, P.: (2018). Convection Initiation
1056 Caused by Heterogeneous Low-Level Jets over the Great Plains, *Mon. Weather*
1057 *Rev.*, 146(8), 2615-2637, doi:10.1175/mwr-d-18-0002.1, 2018.

1058 Guo, J., Liu, B., Gong, W., Shi, L., Zhang, Y., Ma, Y., Zhang, J., Chen, T., Bai, K.,
1059 Stoffelen, A., de Leeuw, G., and Xu, X.: Technical note: First comparison of wind
1060 observations from ESA's satellite mission Aeolus and ground-based radar wind
1061 profiler network of China, *Atmos. Chem. Phys.*, 21, 2945-2958, doi: 10.5194/acp-
1062 21-2945-2021, 2021 (data available at: <https://data.cma.cn>, last access: 11 January
1063 2024).

1064 Guo, X., Guo, J., Chen, T., Li, N., Zhang, F., and Sun, Y.: Revisiting the evolution of
1065 downhill thunderstorms over Beijing: a new perspective from a radar wind profiler
1066 mesonet, *Atmos. Chem. Phys.*, 24(14), 8067-8083, doi:10.5194/acp-24-8067-
1067 2024, 2024.

1068 Guo, X., Guo, J., Zhang, D. L., and Yun, Y.: Vertical divergence profiles as detected
1069 by two wind-profiler mesonets over East China: Implications for nowcasting
1070 convective storms, *Q. J. R. Meteorol. Soc.*, 149(754), 1629-1649.
1071 doi:10.1002/qj.4474, 2023.

1072 Hersbach, H., Bell, B., Berrisford, P., Biavati, G., Horányi, A., Muñoz Sabater, J.,
1073 Nicolas, J., Peubey, C., Radu, R., Rozum, I., Schepers, D., Simmons, A., Soci, C.,
1074 Dee, D. and Thépaut, J.-N.: ERA5 hourly data on pressure levels from 1940 to
1075 present. Copernicus Climate Change Service (C3S) Climate Data Store (CDS),
1076 doi: 10.24381/cds.bd0915c6 (Accessed on 06-05-2024), 2023.

1077 Higgins, R. W., Yao, Y., Yarosh, E. S., Janowiak, J. E., and Mo, K. C.: Influence of the
1078 Great Plains low-level jet on summertime precipitation and moisture transport
1079 over the central United States, *J. Clim.*, 10(3), 481-507, 1997.

1080 Hodges, D., and Pu, Z.: Characteristics and Variations of Low-Level Jets and
1081 Environmental Factors Associated with Summer Precipitation Extremes over the
1082 Great Plains. *J. Clim.*, 32(16), 5123-5144, doi:10.1175/JCLI-D-18-0553.1, 2019.

1083 Holton, J. R.: The diurnal boundary layer wind oscillation above sloping terrain, *Tellus*,
1084 19(2), 200-205, doi: 10.3402/tellusa.v19i2.9766, 1967.

1085 Horinouchi, T., Matsumura, S., Ose, T., and Takayabu, Y. N.: Jet-precipitation relation
1086 and future change of the mei-yu-baiu rainband and subtropical jet in CMIP5
1087 coupled GCM simulations, *J. Clim.*, 32(8), 2247-2259, doi:10.1175/JCLI-D-18-
1088 0426.1, 2019.

1089 Huang, X., Sun, J., and Liu, W.: The interaction between low-level jet evolution and
1090 severe convective rainstorms under topographic effect, *Acta Meteorol. Sin.*, 78(4),
1091 551-567, 2020.

1092 Li, N., and Guo, J.: Data for wind profiles associated with LLJs obtained from RWP
1093 observations during the warm season (April-October) of 2023-2024 in China [Data
1094 set]. Zenodo. <https://doi.org/10.5281/zenodo.17176759>, 2025.

1095 Li, N., Guo, J., Wu, M., Zhang, F., Guo, X., Sun, Y., Zhang Z., Liang L., Chen T.: Low-
1096 level jet and its effect on the onset of summertime nocturnal rainfall in Beijing,
1097 *Geophys. Res. Lett.*, 51, e2024GL110840, doi:10.1029/2024GL11084, 2024.

1098 Li, X., and Du, Y.: Statistical relationships between two types of heavy rainfall and
1099 low-level jets in South China, *J. Clim.*, 34(21), 8549-8566, doi:10.1175/JCLI-D-
1100 21-0121.1, 2021.

1101 Liu, B., Ma, Y., Guo, J. and Wei, G.: Boundary layer heights as derived from ground-
1102 based radar wind profiler in Beijing, *IEEE Trans. Geosci. Remote Sens.*, 57, 8095-
1103 8104, doi:10.1109/TGRS.2019.2918301, 2019.

1104 Liu, X., Luo, Y., Huang, L., Zhang, D. L., & Guan, Z: Roles of double low-level jets in
1105 the generation of coexisting inland and coastal heavy rainfall over south China

Field Code Changed

Field Code Changed

1106 during the presummer rainy season, *Journal of Geophysical Research:*
1107 *Atmospheres*, 125(18), e2020JD032890, 2020.

1108 Luo, Y., Gong, Y., and Zhang, D. L.: Initiation and organizational modes of an extreme-
1109 rain-producing mesoscale convective system along a mei-yu front in East China,
1110 *Mon. Weather Rev.*, 142(1), 203-221, doi:10.1175/MWR-D-13-00111.1, 2014.

1111 Maddox, R. A.: Large-scale meteorological conditions associated with midlatitude,
1112 mesoscale convective complexes, *Mon. Weather Rev.*, 111(7), 1475-1493, 1983.

1113 Marengo, J. A., Soares, W. R., Saulo, C., and Nicolini, M.: Climatology of the low-
1114 level jet east of the Andes as derived from the NCEP-NCAR reanalyses:
1115 Characteristics and temporal variability, *J. Clim.*, 17(12), 2261-2280, 2004.

1116 Markowski, P., & Richardson, Y.: *Mesoscale meteorology in midlatitudes*, John Wiley
1117 & Sons, 2011.

1118 Miao, Y., Guo, J., Liu, S., Wei, W., Zhang, G., Lin, Y., and Zhai, P.: The Climatology
1119 of Low-Level Jet in Beijing and Guangzhou, China, *J. Geophys. Res. Atmos.*,
1120 123(5), 2816-2830. doi:10.1002/2017jd027321, 2018.

1121 Mitchell, M. J., Arritt, R. W., and Labas, K.: A climatology of the warm season Great
1122 Plains low-level jet using wind profiler observations, *Weather Forecast.*, 10(3),
1123 576-591, 1995.

1124 Molod, A., Salmun, H. and Collow, A.B.M.: Annual cycle of planetary boundary layer
1125 heights estimated from wind profiler network data, *J. Geophys. Res. Atmos.*, 124,
1126 6207-6221, doi:10.1029/2018JD030102, 2019.

1127 Monaghan, A. J., Rife, D. L., Pinto, J. O., Davis, C. A., and Hannan, J. R.: Global
1128 precipitation extremes associated with diurnally varying low-level jets, *J. Clim.*,
1129 23(19), 5065-5084, 2010.

1130 Pan, H., and Chen, G.: Diurnal variations of precipitation over North China regulated
1131 by the mountain-plains solenoid and boundary-layer inertial oscillation, *Adv.*
1132 *Atmos. Sci.*, 36(8), 863-884, doi:10.1175/2010JCLI3515.1, 2019.

1133 Pitchford, K. L., and London, J.: The low-level jet as related to nocturnal thunderstorms
1134 over Midwest United States, *J. Appl. Meteorol.*, 1(1), 43-47, 1962.

1135 Rasmussen, K. L., and Houze Jr, R. A.: Convective initiation near the Andes in
1136 subtropical South America, *Mon. Weather Rev.*, 144(6), 2351-2374,
1137 doi:10.1175/MWR-D-15-0058.1, 2016.

1138 Reif, D. Q., and Bluestein, H.: A 20-year climatology of nocturnal convection initiation
1139 over the central and southern great plains during the warm season, *Mon. Weather*
1140 *Rev.*, 145, 1615-1639, doi:10.1175/MWR-D-16-0340.1, 2017.

1141 Roots, M., Sullivan, J. T., and Demoz, B.: Mid-Atlantic nocturnal low-level jet
1142 characteristics: a machine learning analysis of radar wind profiles, *Atmos. Meas.*
1143 *Tech.*, 18(5), 1269-1282, doi:10.5194/amt-18-1269-2025, 2025.

1144 Stensrud, D. J.: Importance of low-level jets to climate: A review, *J. Clim.*, 1698-1711,
1145 1996.

1146 Subrahmayam, K. V., Udupa, S. R., Kumar, K. K., Ramana, M. V., Srinivasulu, J., and
1147 Bothale, R. V.: Prediction of zonal wind using machine learning algorithms:
1148 Implications to future projections of Indian monsoon jets, *J. Indian Soc. Remote*
1149 *Sens.*, 52(2), 371-381, 2024.

1150 Sun, S. Q., Zhai, G. H., and Lorenzo, D. O.: The relationship between large-scale low-
1151 level jet over east asia and monsoon as well as cross-equatorial currents in
1152 summer, *Acta Meteorol. Sin.*, 1(1), 43-50, 1986.

1153 Trier, J. W. Wilson, D. A. Ahijevych, and R. A. Sobash : Mesoscale vertical motions
1154 near nocturnal convection initiation in PECAN, *Mon. Weather Rev.*, 145, 2919-
1155 2941, doi:10.1175/MWR-D-17-0005.1, 2017.

1156 Trier, S. B., Davis, C. A., Ahijevych, D. A., Weisman, M. L., and Bryan, G. H.:
1157 Mechanisms supporting long-lived episodes of propagating nocturnal convection
1158 within a 7-day WRF model simulation, *J. Atmos. Sci.*, 63(10), 2437-2461, doi:
1159 10.1175/JAS3768.1, 2006.

1160 Tuttle, J. D., and Davis, C. A.: Corridors of warm season precipitation in the central
1161 United States. *Mon. Weather Rev.*, 134(9), 2297-2317, doi:10.1175/MWR3188.1,
1162 2006.

1163 Uccellini, L. W., and D. R. Johnson: The coupling of upper and lower tropospheric jet
1164 streaks and implications for the development of severe convective storms.

1165 Monthly Weather Review, 107, 682-703, doi: 10.1175/1520-
1166 0493(1979)107,0682:TCOUAL.2.0.CO;2, 1979.

1167 Walters, C. K., Winkler, J. A., Shadbolt, R. P., van Ravensway, J., and Bierly, G. D.:
1168 A long-term climatology of southerly and northerly low-level jets for the central
1169 United States, *Ann. Assoc. Am. Geogr.*, 98(3), 521-552, 2008.

1170 Wang, D., Zhang, Y., and Huang, A.: Climatic features of the south-westerly low-level
1171 jet over southeast China and its association with precipitation over east China,
1172 *Asia-Pac. J. Atmos. Sci.*, 49(3), 259-270, doi:10.1007/s13143-013-0025-y, 2013.

1173 Wang, W. C., Gong, W., and Wei, H.: A regional model simulation of the 1991 severe
1174 precipitation event over the Yangtze-Huai River valley. Part I: Precipitation and
1175 circulation statistics, *J. Clim.*, 13(1), 74-92, doi:10.1175/1520-
1176 0442(2000)013<0074:ARMSOT>2.0.CO;2, 2000.

1177 Weckwerth, T. M., and Wakimoto, R. M.: The initiation and organization of convective
1178 cells atop a cold-air outflow boundary, *Mon. Weather Rev.*, 120(10), 2169-2187,
1179 doi:10.1175/1520-0493(1992)120,2169:TIAOOC.2.0.CO;2, 1992.

1180 Weckwerth, T. M., Hanesiak, J., Wilson, J. W., et al.: Nocturnal convection initiation
1181 during PECAN 2015, *Bull. Am. Meteorol. Soc.*, 100(11), 2223-2239,
1182 doi:10.1175/BAMS-D-18-0299.1, 2019.

1183 Wei, W., Zhang, H. S., and Ye, X. X.: Comparison of low-level jets along the north
1184 coast of China in summer, *J. Geophys. Res. Atmos.*, 119(16), 9692-9706.
1185 doi:10.1002/2014jd021476, 2014.

1186 Weisman, M. L., Trapp, R. J., Romine, G. S., Davis, C., Torn, R., Baldwin, M., Bosart,
1187 L., Brown, J., Coniglio, M., Dowell, D., Evans, A. C., Galarneau, T. J., Haggerty,
1188 J., Hock, T., Manning, K., Roebber, P., Romashkin, P., Schumacher, R., Schwartz,
1189 C. S., Sobash, R., Stensrud, D., and Trier, S. B.: The mesoscale predictability
1190 experiment (MPLEX), *Bull. Am. Meteorol. Soc.*, 96(12), 2127-2149,
1191 doi:10.1175/bams-d-13-00281.1, 2015.

1192 Whiteman, C. D., Bian, X., and Zhong, S.: Low-level jet climatology from enhanced
1193 Rawinsonde observations at a site in the southern Great Plains, *J. Appl. Meteorol.*,

1194 36(10), 1363-1376, doi:10.1175/1520-
1195 0450(1997)036%3C1363:LLJCFE%3E2.0.CO;2, 1997.

1196 Xia, R., and Zhao, S.: Diagnosis and modeling of meso-scale systems of heavy rainfall
1197 in warm sector ahead of front in South China (middle part of Guangdong province)
1198 in June 2005, *Chin. J. Atmos. Sci.*, 33(3), 2009.

1199 Xue, M., Luo, X., Zhu, K., Sun, Z., and Fei, J.: The controlling role of boundary layer
1200 inertial oscillations in Meiyu frontal precipitation and its diurnal cycles over
1201 China, *J. Geophys. Res. Atmos.*, 123(10), 5090-5115,
1202 doi:10.1029/2018JD028368, 2018.

1203 Yan, Y., Cai, X., Wang, X., Miao, Y., and Song, Y.: Low-level jet climatology of China
1204 derived from long-term radiosonde observations, *J. Geophys. Res. Atmos.*,
1205 126(20), e2021JD035323, doi:10.1029/2021JD035323, 2021.

1206 Yu, R., Li, J., Chen, H., and Yuan, W.: Progress in studies of the precipitation diurnal
1207 variation over contiguous China, *J. Meteorol. Res.*, 28(5), 877-902,
1208 doi:10.1007/s13351-014-3272-7, 2014.

1209 Zamora, R.J., Shapiro, M.A. and Doswell, C.A., III.: The diagnosis of upper
1210 tropospheric divergence and ageostrophic wind using profiler wind observations,
1211 *Mon. Weather Rev.*, 115, 871-884, doi:10.1175/1520-0493(1987)1152.0.CO;2,
1212 1987.

1213 Zhang, F., Zhang, Q., Sun, J., and Xu, J.: Convection initiation during the Meiyu
1214 environment in the Yangtze-Huai River basin of China, *J. Geophys. Res. Atmos.*,
1215 128(9), e2022JD038077, doi:10.1029/2022JD038077, 2023.

1216 Zhang, M., and Meng, Z.: Warm-sector heavy rainfall in southern China and its WRF
1217 simulation evaluation: A low-level-jet perspective, *Mon. Weather Rev.*, 147(12),
1218 4461-4480, doi:10.1175/MWR-D-19-0110.1, 2019.

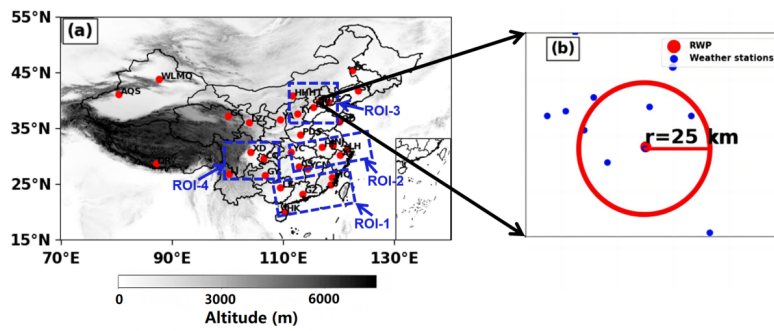
1219 Zhang, Y., Xue, M., Zhu, K., and Zhou, B.: What is the main cause of diurnal variation
1220 and nocturnal peak of summer precipitation in Sichuan Basin, China? the key role
1221 of boundary layer low-level jet inertial oscillations, *J. Geophys. Res. Atmos.*,
1222 124(5), 2643-2664, doi:10.1029/2018jd029834, 2019.

1223 Zhao, Y., Liao, J., Zhang, Q., Chen, J., Gong, X., Shi, Y., Shi, M., Yang, D., Fan, S.,
1224 Zhou, X., Cao, L., and Hu, K.: Development of China Ground Climate Normal
1225 Value Dataset from 1991 to 2020, Chinese Journal of Atmospheric Sciences (in
1226 Chinese), 48(2), 555–571, doi:10.3878/j.issn.1006-9895.2204.22010, 2024.
1227
1228

Table 1. Table of Representative Radar Wind Profiler Stations in Mainland China

Region	Station	Longitude (°)	Latitude (°)	Altitude (m)	
ROI-1	58839	MQ	118.86	26.22	160.70
	59046	LZ	109.46	24.36	314.40
	59137	JJ	118.54	24.81	124.80
	59287	GZ	113.48	23.21	65.00
	59758	HK	110.25	19.99	69.00
ROI-2	57461	YC	111.36	30.74	253.80
	57687	CS	112.79	28.11	119.00
	57793	YCN	114.36	27.79	132.00
	58238	BJ	118.90	31.93	40.60
	58321	HF	117.03	31.57	50.00
	58367	LH	121.47	31.18	5.00
	58459	XS	120.29	30.18	48.80
ROI-3	53463	HHHT	111.68	40.82	1152.10
	53772	TY	112.58	37.62	785.00
	54511	BJ	116.47	39.81	31.50
	54534	TS	118.10	39.65	23.20
	54602	BD	115.48	38.73	16.80
ROI-4	57816	GY	106.73	26.59	1197.60
	56290	XD	104.18	30.77	514.00
	56651	LJ	100.22	26.85	2382.40
Other stations	50936	BC	122.47	45.36	156.00
	51463	WLMQ	87.65	43.79	935.00
	51628	AKS	80.38	41.12	1107.10
	52754	GC	100.08	37.2	3301.50
	52889	LZ	103.89	36.06	1519.20
	57516	CQ	106.46	29.57	260.00
	53845	YA	109.45	36.58	1180.40
	54342	SY	123.51	41.73	50.00
	54857	QD	120.13	36.23	12.00
	55664	DR	87.07	28.63	4302.00
	57171	PDS	113.12	33.77	142.00

1230 Figures
1231



1232

1233 Figure.1 (a) Spatial distribution of 31 Radar Wind Profiler (RWP) stations (red dots)
1234 across China, with four regions of interest (ROIs) demarcated by blue dashed boxes:
1235 ROI-1, ROI-2, ROI-3, and ROI-4. (b) Schematic of spatial co-location: Beijing
1236 Observatory's RWP (red circle) and rain gauges (blue dots) within a 25-km radius

Deleted: ack

1237

1238

1239

1240

1241

1242

1243

1244

1245

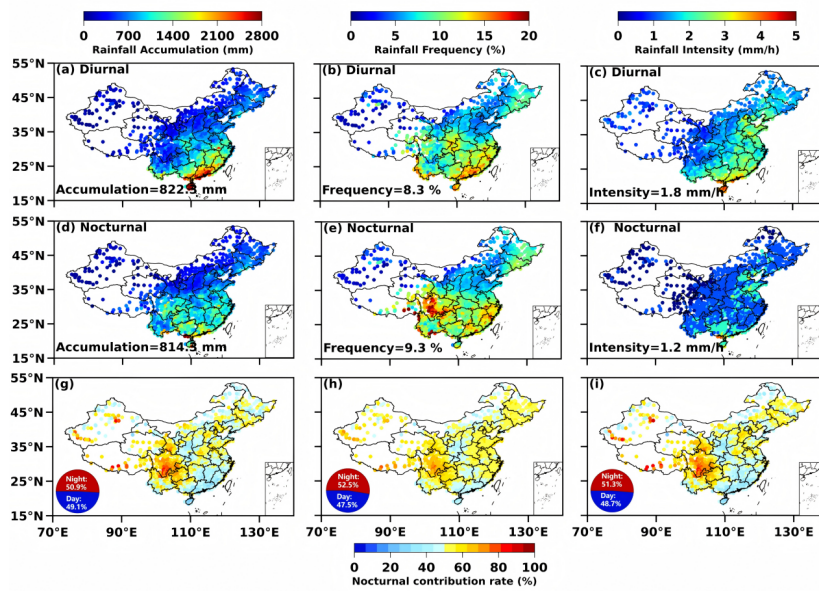
1246

1247

1248

1249

1250

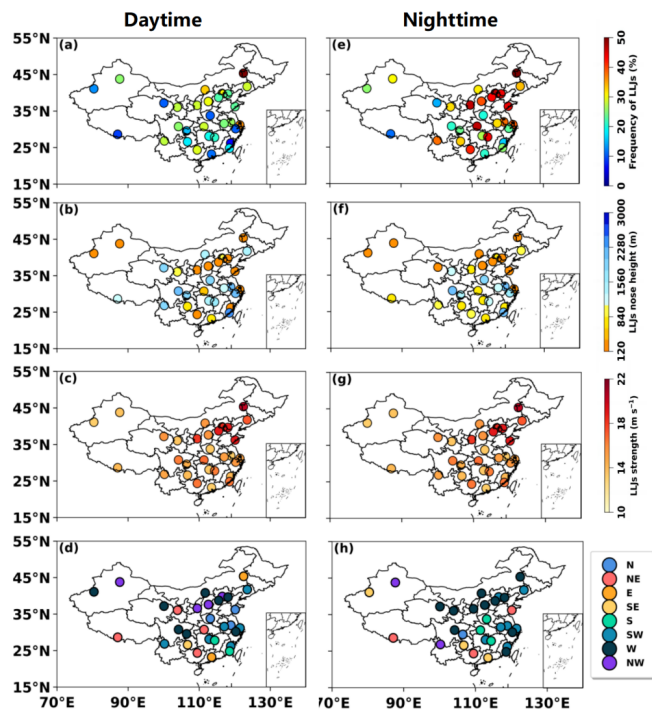


1252

1253 Figure 2. (a–c) Spatial distributions of accumulated rainfall (mm), rainfall frequency
 1254 (%) and rainfall intensity (mm/h) in the daytime from April to October in 2023–2024.
 1255 The numbers in the upper left corner represent the national average; (d–f) the same as
 1256 (a–c), but in the nighttime; (g–i) Nocturnal contribution ratios of accumulated rainfall,
 1257 frequency, and occurrence frequency of heavy rainfall (>75th percentile intensity). The
 1258 pie charts illustrate the relative contribution rates of daytime (blue) and nighttime (red)
 1259 at the national scale

1260

1261



1262

1263 Figure 3. (a–d) Spatial distribution of occurrence frequency, height, strength, and the
 1264 dominant wind direction of LLJs observed by 31 RWP stations during April–October
 1265 from 2023 to 2024 in the daytime. (e–h) Same as (a–d), but in the nighttime.

1266

1267

1268

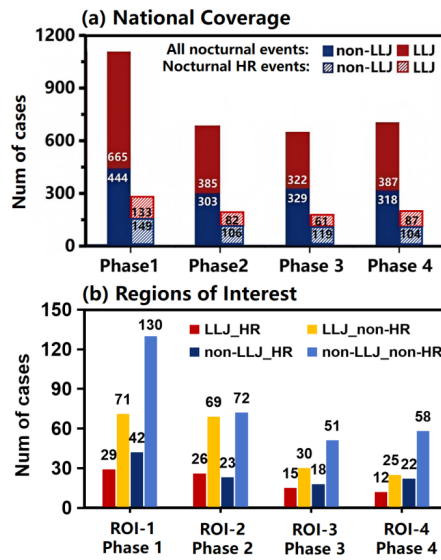
1269

1270

1271

1272

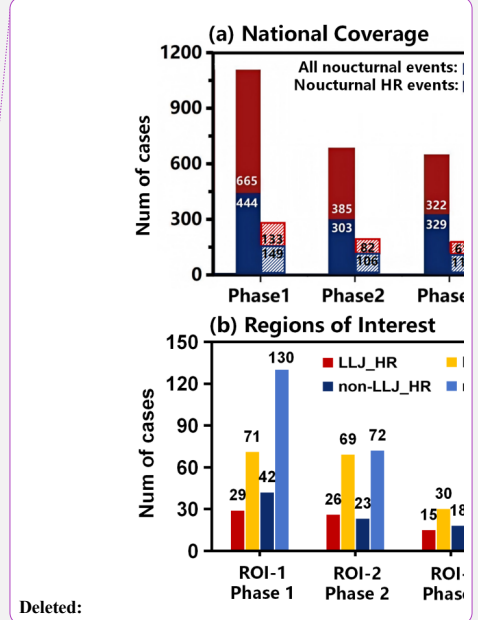
1273



1274

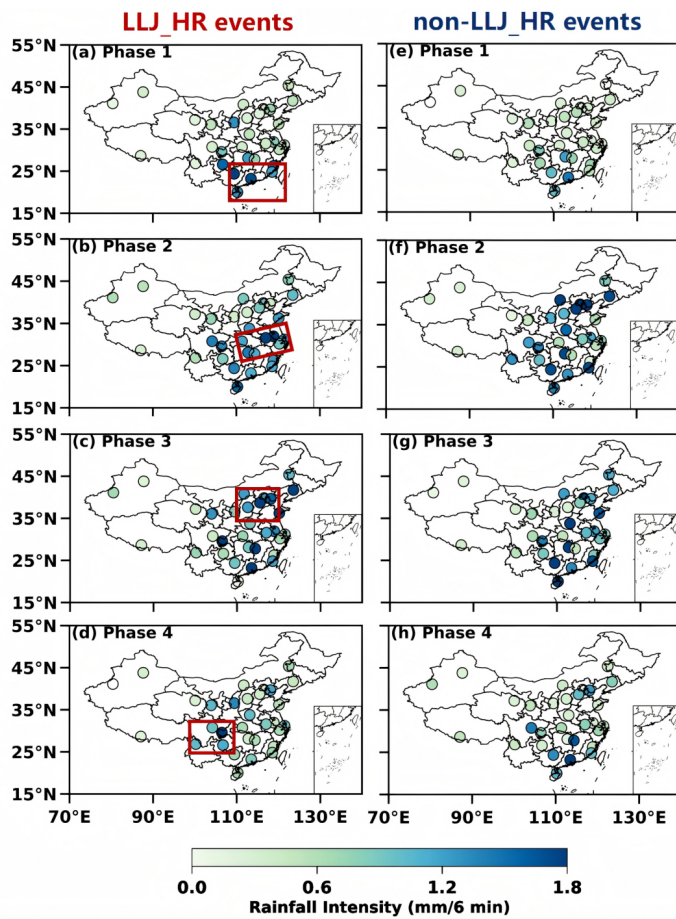
1275 Figure 4. Statistics of all nocturnal rainfall events (solid-filled bars) and nocturnal heavy
 1276 rainfall (HR; diagonally striped bars) events across China during four phases,
 1277 categorized into LLJ events (red) and non-LLJ events (blue). (b) Statistics of nocturnal
 1278 rainfall events within the four ROIs (ROI-1 to ROI-4) during their corresponding
 1279 phases, categorized into four types: LLJ_HR (red), LLJ_non-HR (yellow), non-
 1280 LLJ_HR (dark blue), and non-LLJ_non-HR (light blue) events.

1281



Deleted:

Deleted: all



1284

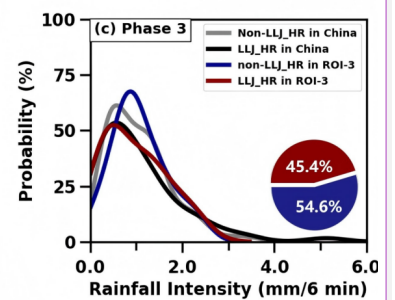
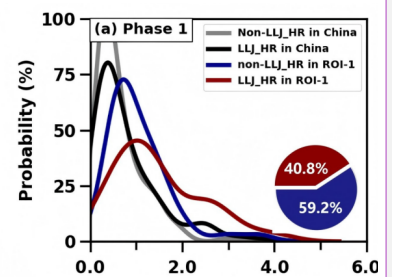
1285 Figure 5. (a–d) Spatial distributions of site-averaged rain rate (mm/6 min) for nocturnal
 1286 LLJ_HR events during the warm season from Phase 1 to Phase 4 across China; (e–h)

1287 Same as (a–d), but for non-LLJ_HR events. The red frame indicates four ROIs.

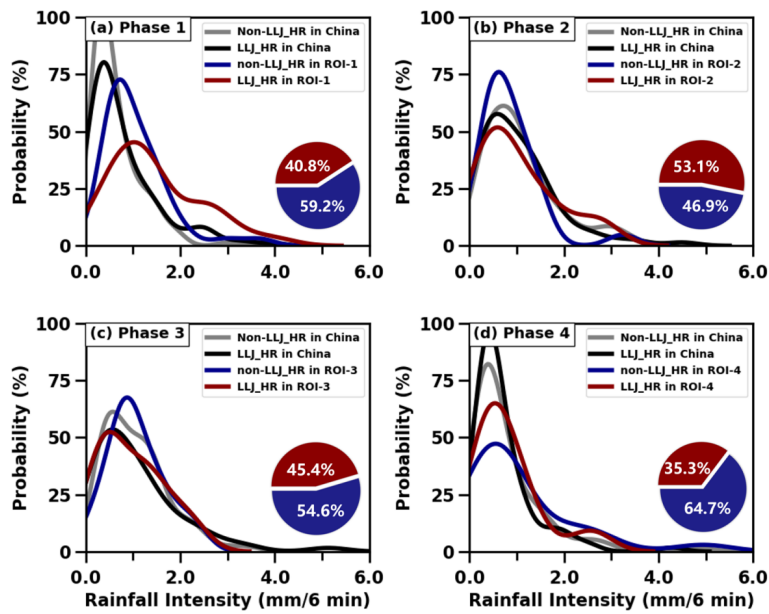
1288

1289

Deleted: average



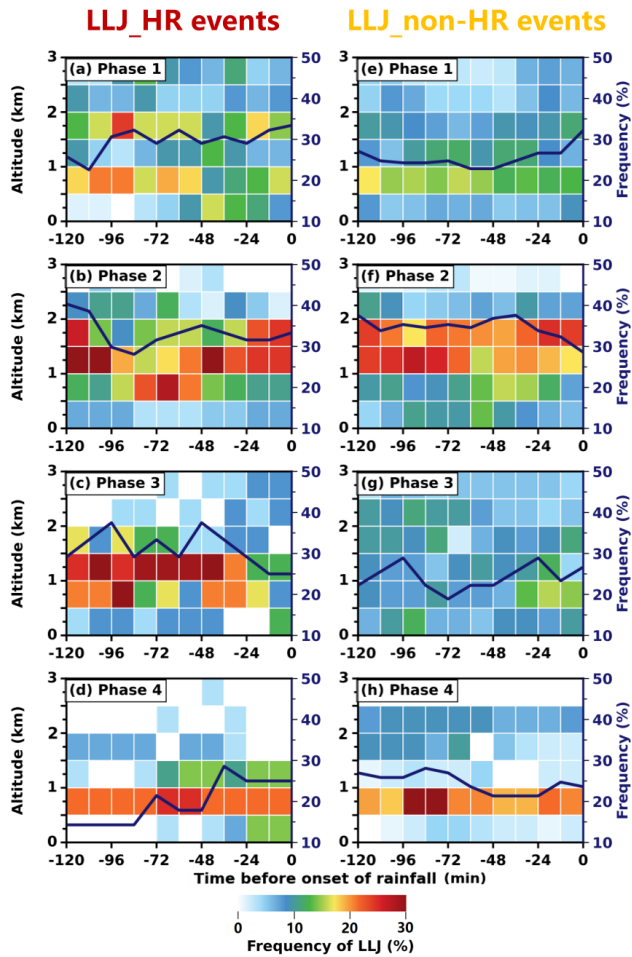
Deleted:



1292

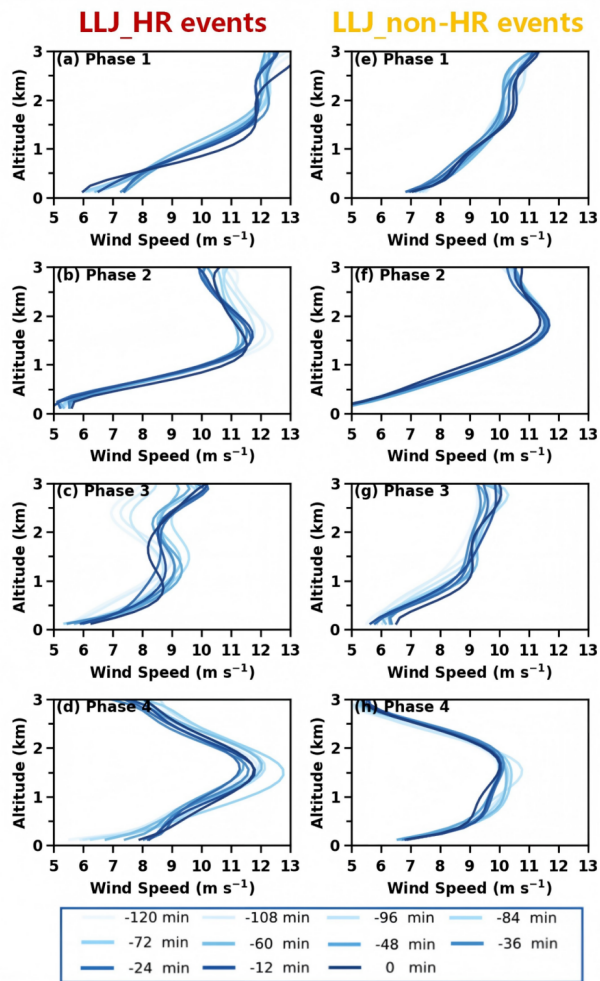
1293 Figure 6. (a) Probability density distributions of average rain rate (mm/6 min) for
 1294 LLJ_HR events (black solid lines) and non-LLJ_HR events (gray solid lines) across
 1295 China during Phase 1, and specifically in ROI-1 for LLJ_HR events (red solid lines)
 1296 and non-LLJ_HR events (blue solid lines). (b-d) the same as panel (a), but for
 1297 comparisons between national-scale and other regional-scale events in ROI-2 during
 1298 Phase 2, ROI-3 during Phase 3, and ROI-4 during Phase 4. The pie chart at the lower
 1299 right shows the proportion distribution of LLJ_HR (red) and non-LLJ_HR (blue) events
 1300 in these key regions during each period

1301



1302

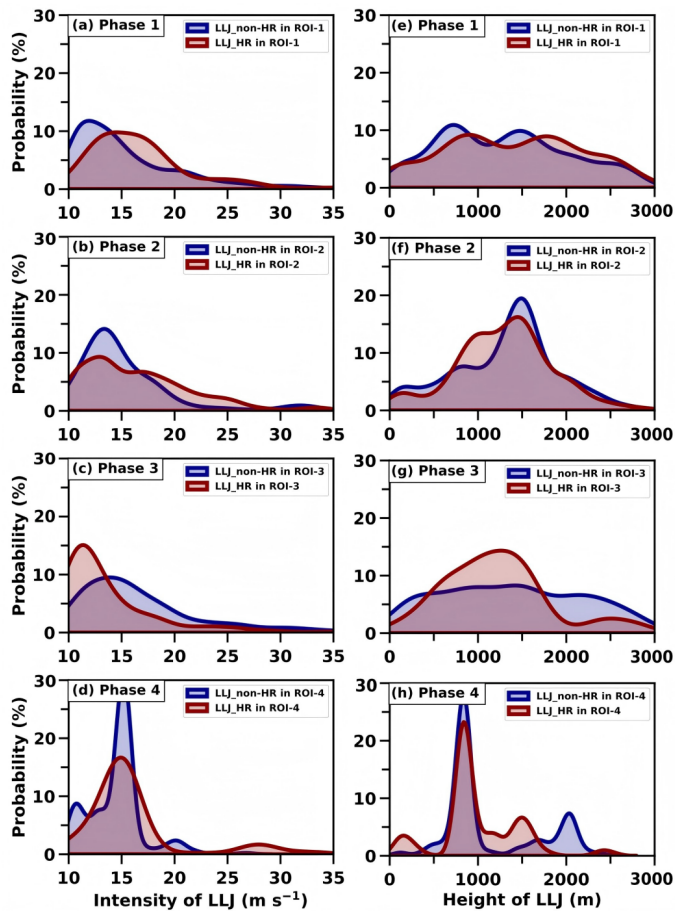
1303 Figure 7. Time-height evolution of LLJ occurrence frequency (color shading, every 12
 1304 min, within 500 m vertical bins) detected by RWP with 2 hours preceding nocturnal
 1305 rainfall in LLJ_HR events in (a) ROI-1 during Phase 1, (b) ROI-2 during Phase 2, (c)
 1306 ROI-3 during Phase 3, and (d) in ROI-4 during Phase 4. Dark blue solid lines denote
 1307 accumulated LLJ frequency over 0–3 km latitude. (e-h) Same as (a-d), but for LLJ_
 1308 non-HR events



1309

1310 Figure 8. (a-d) Evolution of RWP-detected mean wind profiles of LLJs (blue solid lines,
 1311 every 12 min) within 2 hours preceding nocturnal rainfall in LLJ_HR events in (a) ROI-
 1312 1 during Phase 1, (b) ROI-2 during Phase 2, (c) ROI-3 during Phase 3, and (d) in ROI-
 1313 4 during Phase 4. (e-h) Same as (a-d), but for LLJ_non-HR events

1314



Deleted: ¶

Formatted: Font: (Asian) +Body Asian (SimSun)

Formatted: Centered

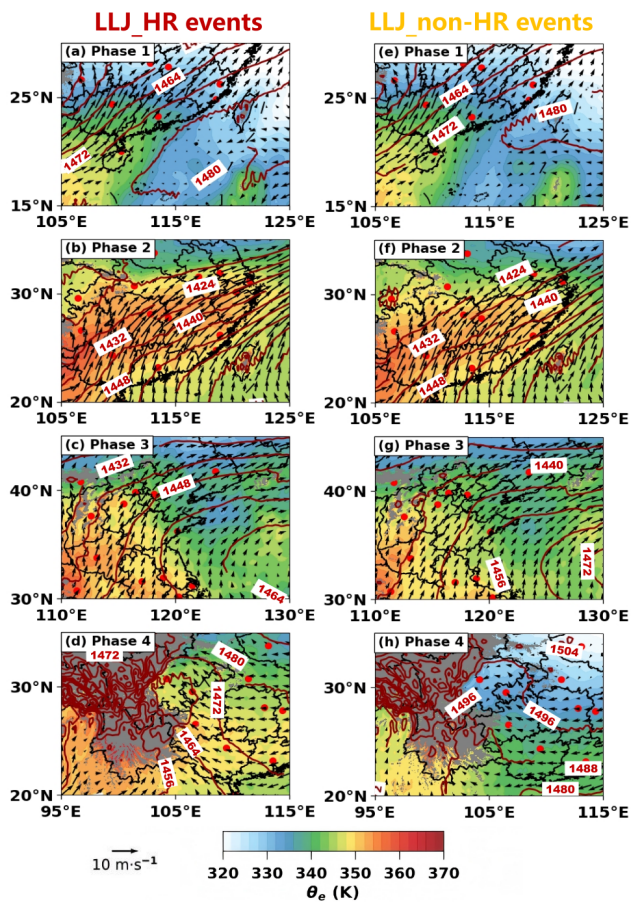
1315

1316 Figure 9. Probability density distributions of jet core intensity from RWP observations
 1317 within 2 hours preceding nocturnal rainfall in LLJ_HR events in (a) ROI-1 during Phase
 1318 1, (b) ROI-2 during Phase 2, (c) ROI-3 during Phase 3, and (d) in ROI-4 during Phase
 1319 4. (e-h) Same as (a-d), but for the height of LLJs

1320

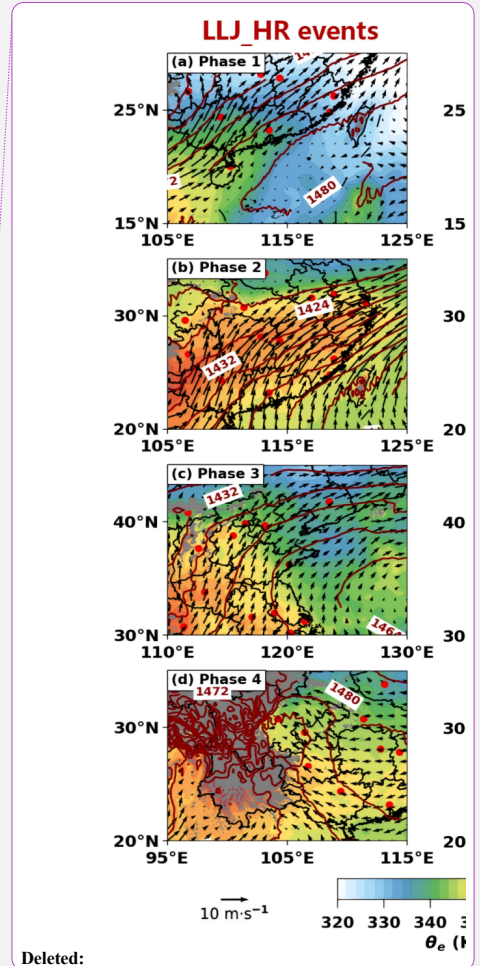
1321

1322

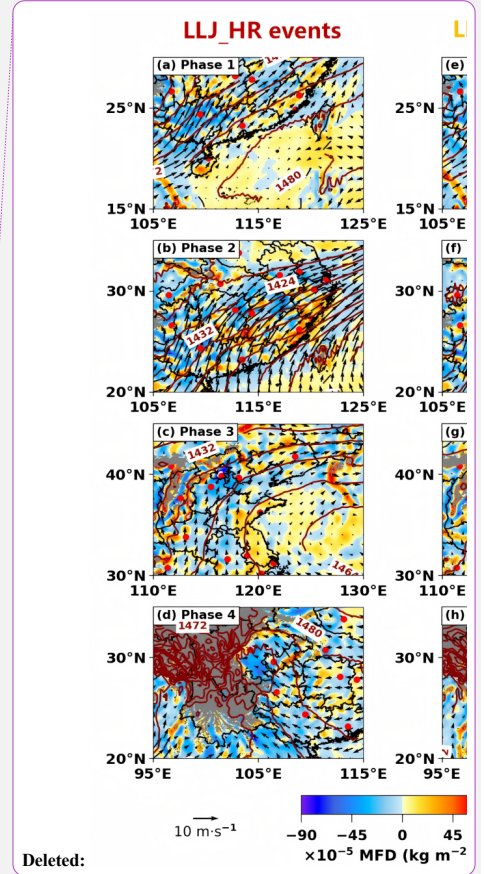
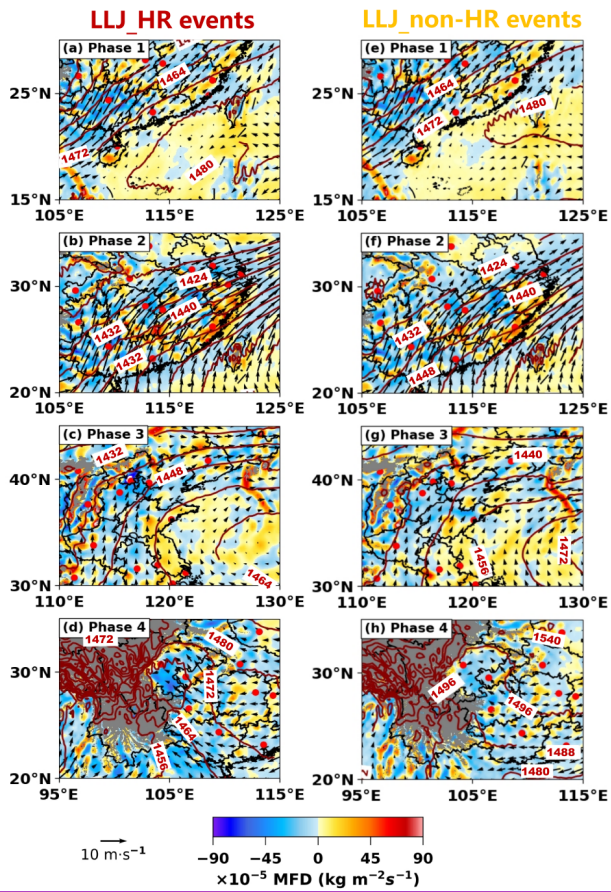


1324

1325 Figure 10. Distributions of equivalent potential temperature (shading, unit: K) at 850
 1326 hPa, superimposed with 850 hPa horizontal wind vectors (black arrows) and
 1327 geopotential height contours (red solid lines), for LLJ_HR events within 1-hour time
 1328 window preceding nocturnal rainfall onset in (a) ROI-1 during Phase 1, (b) ROI-2
 1329 during Phase 2, (c) ROI-3 during Phase 3, and (d) in ROI-4 during Phase 4. Gray
 1330 shading denotes terrain elevation exceeding 850 hPa level. The reference vector (10
 1331 m s⁻¹) is shown at the lower-left corner. (e-h) Same as (a-d), but for LLJ_non-HR events



Deleted:

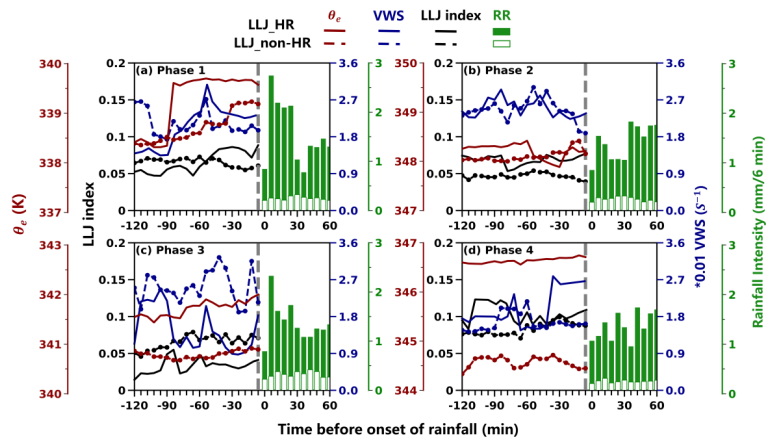


1333

1334 Figure 11. Same as Figure 10, but showing the integrated moisture flux divergence
 1335 (shading, unit: $\text{kg m}^{-2} \text{s}^{-1}$) between 1000–700 hPa at 1 hour prior to preceding
 1336 nocturnal rainfall onset

1337

1338



1340

1341 Figure 12. Temporal evolution of surface equivalent potential temperature (θ_e , red
 1342 lines), vertical wind shear (VWS, blue lines), and LLJ index (black lines) averaged
 1343 within 2 hours preceding nocturnal rainfall for LLJ_HR events (solid lines) and
 1344 LLJ_non-HR events (dashed lines) in (a) ROI-1 during Phase 1, (b) ROI-2 during Phase
 1345 2, (c) ROI-3 during Phase 3, and (d) in ROI-4 during Phase 4. Green bars denote 6-min
 1346 averaged rain rate (mm/6 min) after LLJ_HR (solid bars) and LLJ_non-HR (open bars)
 1347 events onset

1348

1349

1350

1351

